nature COMMUNICATIONS

ARTICLE

https://doi.org/10.1038/s41467-021-25980-y OPEN

Efficient propyne/propadiene separation by microporous crystalline physiadsorbents

Yun-Lei Peng[1,2], Ting Wang[1], Chaonan Jin[3], Cheng-Hua Deng[2], Yanming Zhao[4], Wansheng Liu[1], Katherine A. Forrest[5], Rajamani Krishna[6], Yao Chen[3], Tony Pham[5], Brian Space[5], Peng Cheng[1,7,8], Michael J. Zaworotko[2] & Zhenjie Zhang[1,7,8]✉

Selective separation of propyne/propadiene mixture to obtain pure propadiene (allene), an essential feedstock for organic synthesis, remains an unsolved challenge in the petrochemical industry, thanks mainly to their similar physicochemical properties. We herein introduce a convenient and energy-efficient physisorptive approach to achieve propyne/propadiene separation using microporous metal-organic frameworks (MOFs). Specifically, HKUST-1, one of the most widely studied high surface area MOFs that is available commercially, is found to exhibit benchmark performance (propadiene production up to 69.6 cm^3/g, purity > 99.5%) as verified by dynamic breakthrough experiments. Experimental and modeling studies provide insight into the performance of HKUST-1 and indicate that it can be attributed to a synergy between thermodynamics and kinetics that arises from abundant open metal sites and cage-based molecular traps in HKUST-1.

[1] College of Chemistry, Nankai University, Tianjin 300071, People's Republic of China. [2] Department of Chemical Sciences, Bernal Institute, University of Limerick, Limerick V94 T9PX, Republic of Ireland. [3] State Key Laboratory of Medicinal Chemical Biology, Nankai University, Tianjin 300071, People's Republic of China. [4] Henan Institute of Advanced Technology, Zhengzhou University, Zhengzhou 450052, People's Republic of China. [5] Department of Chemistry, University of South Florida; 4202 East Fowler Avenue, CHE205, Tampa, FL 33620-5250, USA. [6] Van't Hoff Institute for Molecular Sciences, University of Amsterdam; Science Park 904, 1098 XH Amsterdam, The Netherlands. [7] Key Laboratory of Advanced Energy Materials Chemistry (MOE), Nankai University, Tianjin 300071, People's Republic of China. [8] Renewable Energy Conversion and Storage Center, Frontiers Science Center for New Organic Matter, Nankai University, Tianjin 300071, People's Republic of China. ✉email: zhangzhenjie@nankai.edu.cn

Propadiene ($CH_2=C=CH_2$), the parent compound of allenes, is an important feedstock for organic synthesis. For instance, propadiene can serve as a chiral building block or as a useful reagent for cycloaddition reactions to form cyclobutane or trimethylenecyclohexane derivatives[1–5]. The combination of propadiene with inexpensive and environmentally benign hydrosilanes can serve as a replacement for stoichiometric quantities of allylmetal reagents, which are required in most enantioselective ketone allylation reactions[6]. Propadiene dimer (unsaturated four-membered ring hydrocarbons) prepared from prodadiene is also a useful and versatile starting material for valuable-added products[7]. At present, pure propadiene is produced via chemical synthesis with low yields, high energy consumption, and undesirable waste by-products[8–10]. A alternative approach to produce pure propadiene is urgently needed. Hydrocarbon cracking is among the largest-scale chemical processes in operation worldwide, converting over 500 million metric tons of feedstock per year to products such as α-olefins[11]. Propadiene is a by-product that constitutes 0.3–0.6 mass percent (wt %) of the total output and roughly 6 mole percent (mol%) of the crude C3 fraction (Fig. 1a)[12]. Propadiene is often available as a mixture with other gases such as propyne, from which it is difficult to separate due to their similar molecular sizes (difference < 0.2 Å) and close boiling points (difference = 10.8 °C) (Fig. 1b). Currently, there is still no effective pathway to purify propadiene[13–16], and propadiene-containing mixtures are generally processed as fuel to burn directly in industry which causes a lot of waste.

Physisorptive separation using porous sorbents has been of interest for some time[17–20]. In principle, sorbents can supercede traditional distillation separation methods and offer low energy consumption with easy operation and excellent safety. In the past two decades, metal-organic frameworks (MOFs), also known as porous coordination polymers, have emerged as a promising class of physisorbents for the capture, separation, and purification of light hydrocarbon gas mixtures[21,22]. Based on the concept of crystal engineering, MOFs can be fine-tuned in terms of pore size and pore chemistry[23–26]. in a manner that is infeasible for traditional porous sorbents such as activated carbon and zeolites[27,28]. The separation of gas mixtures via physisorption depends on several factors, including polarity, size, and shape of gas molecules. In general, the greater the difference in these factors, the easier it is to achieve efficient separation. The physisorptive separation of industrially gas mixtures such as ethylene/ethane[29–33], ethylene/acetylene[19,34–36], acetylene/carbon dioxide[37–39], propylene/propyne[40,41], and propane/propylene[20,42,43] exemplify what seemed intractable challenges that have recently been addressed by microporous MOFs with suitable pore size and chemistry to enable selective binding. Propyne/propadiene separation, however, (Fig. 2a) remains unresolved. Whereas thermodynamically driven separation (Fig. 2b) has proven effective for other separations, it is mitigated here by the almost identical polarizability of propyne *vs.* propadiene (55.5×10^{-25} cm^3 vs. 56.9×10^{-25} cm^3)[44–46]. These critical requirements cause difficulty for separation propyne/propadiene mixtures[47].

Here, we address the challenge of propyne/propadiene separation and report a thermodynamic-kinetic dual-drive separation strategy (Fig. 2d) using microporous MOF adsorbents with dense open metal sites (OMSs) and cage-based molecule traps which would offer the needed performance driven by two factors: (i) The C≡C moiety in propyne offers distinct binding to OMSs. (ii) The pore shapes of adsorbents can be adjusted to control gas diffusion to enhance the dynamic screening effect. Our study reveals that microporous MOFs with both a high-density of OMSs and restricted cage-based molecule traps, as exemplified by HKUST-1 and MOF-505, exhibit the best separation performance by comprehensive comparison of a range of candidate sorbent. Importantly, HKUST-1 is one of the few MOFs that has been manufactured at an industrial scale with current production methodology offering a space-time yield of 400,000 kg m^{-3} day^{-1} [48].

Results and discussion

Structure and basic characterizations. We selected a sorbent library comprising traditional porous materials (activated carbon and zeolites) and three types of MOFs (14 different sorbents) classified as follows: (I) MOFs with OMSs, including HKUST-1, MOF-505, Mg-MOF-74, NKMOF-1-Ni, MIL-100-Cr, MIL-100-Fe and MIL-101-Cr; (II) Hybrid ultramicroporous MOFs with strong binding sites (e.g., SiF_6^{2-} and $NbOF_5^{2-}$), including SIFSIX-2-Cu-i, SIFSIX-3-Ni, UTSA-200 (SIFSIX-14-Cu-i) and ZU-62; (III) MOFs without strong binding sites, including UiO-66,

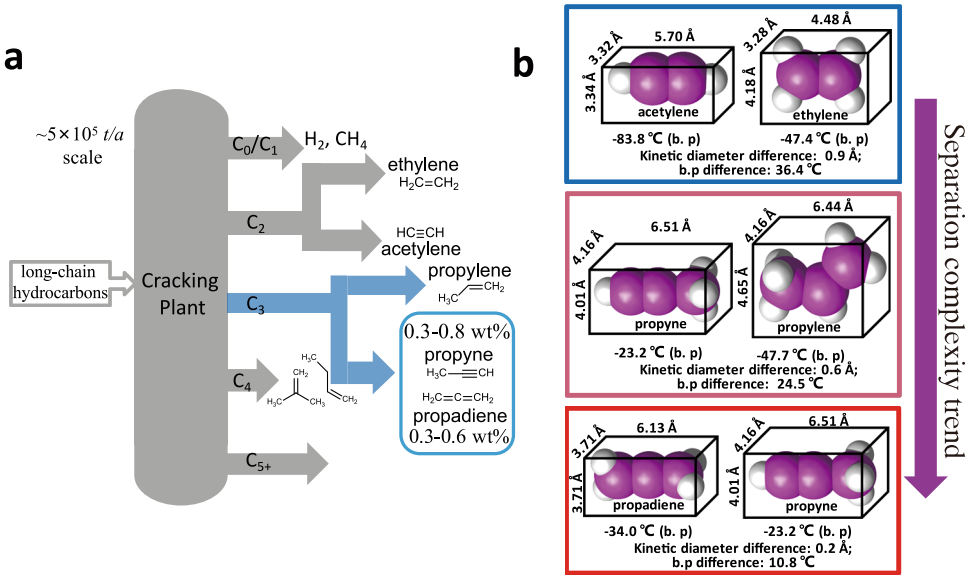

Fig. 1 The major sources and separation complexity of light hydrocarbons. a Schematic diagram of the hydrocarbon cracking process. **b** Comparison of molecular size, kinetic diameter, and b.p difference of acetylene and ethylene, propyne and propylene and propyne and propadiene.

UiO-67, and ZIF-8 (Supplementary Table 1 for detailed structural parameters). Screening of this library was conducted by dynamic breakthrough tests to find the best performing candidates for propyne/propadiene separation. In addition, the equilibrium adsorption isotherms, simulated gas sorption studies, and kinetic adsorption behavior of the library were evaluated (Fig. 3). Activated carbon and zeolites were obtained via commercial sources. All MOFs samples in this study were prepared according to the previous procedures reported in the literature or using appropriately modified procedures. Powder X-ray diffraction (PXRD), BET surface area measurement, and scanning electron microscopy (SEM) data (Supplementary Figs. 1–6) confirmed that all MOFs possessed high crystallinity and the expected sorption parameters.

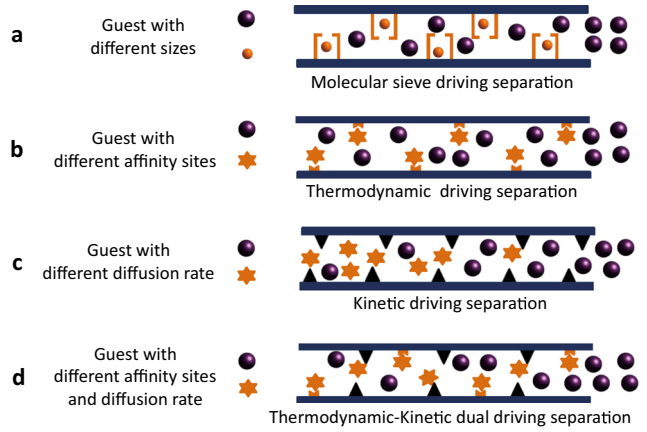

Fig. 2 Illustration of adsorption separation mechanisms in physisorbents. **a** Molecular sieving. **b** Thermodynamically driven separation. **c** Kinetically driven mechanism. **d** Thermodynamic-kinetic dual-driving mechanism.

The dynamic actual breakthrough experiment. Dynamic breakthrough experiments are the most direct and reliable way to evaluate sorption separation performance. Breakthrough experiments of propyne/propadiene mixtures that simulate vacuum swing adsorption processes were conducted on a custom-built separation apparatus in which propyne/propadiene (50/50, v/v) mixtures were used as feed gas (Supplementary Fig. 7). The dynamic breakthrough was performed using a packed column of the activated sorbent under a 2.0 mL/min flow of propyne/propadiene (50/50, v/v) at 298 K. Experimental results are presented in Fig. 4 and Supplementary Fig. 8. The breakthrough results revealed no separation for activated carbon and zeolites whereas some MOFs with OMSs were effective. As revealed by Fig. 4, propadiene was eluted through the adsorption bed while propyne was retained, affording >99.5% pure propadiene. The retention time of propyne after breakthrough was 87 min/g for HKUST-1 and 51 min/g for MOF-505. Although Mg-MOF-74 and NKMOF-1-Ni, other MOFs with a high-density of OMSs, also exhibited separation, retention times were only 15 and 6 min/g (propadiene purity > 99.5%, Fig. 4). Mesoporous MOFs with OMSs (MIL-100-Cr, MIL-100-Fe and MIL-101-Cr) showed no separation effect (Supplementary Fig. 8a–c). Type-II MOFs with

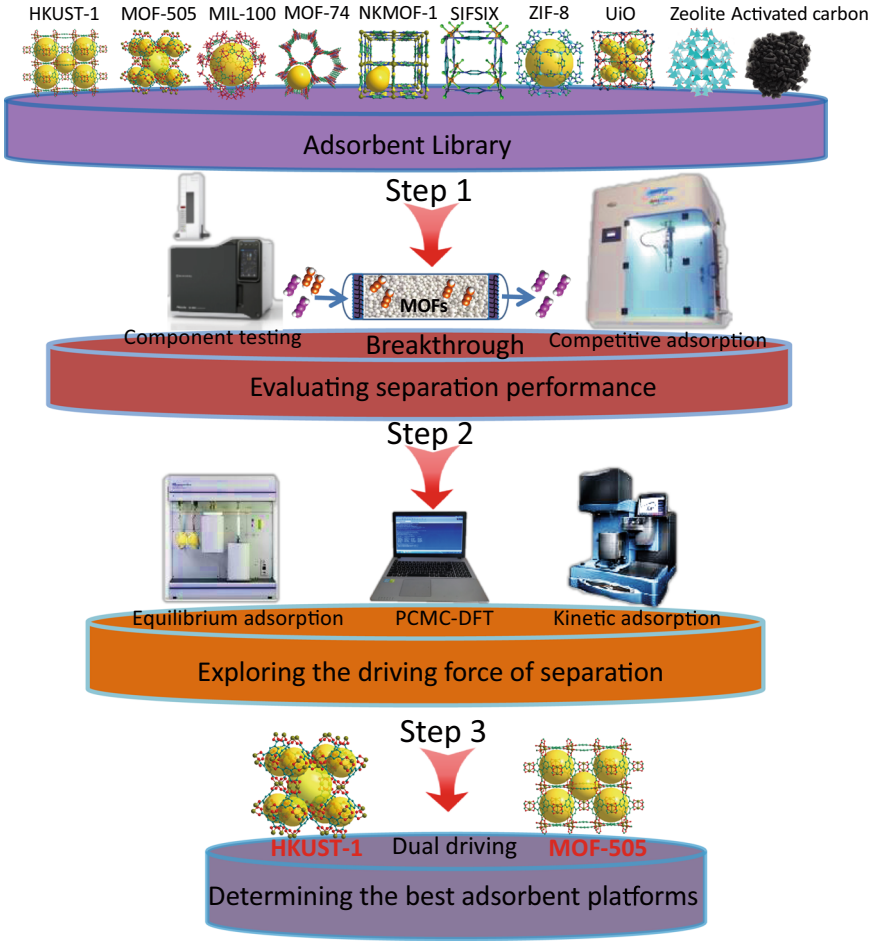

Fig. 3 Illustration of the assay package used herein for determining propyne/propadiene separation performance.

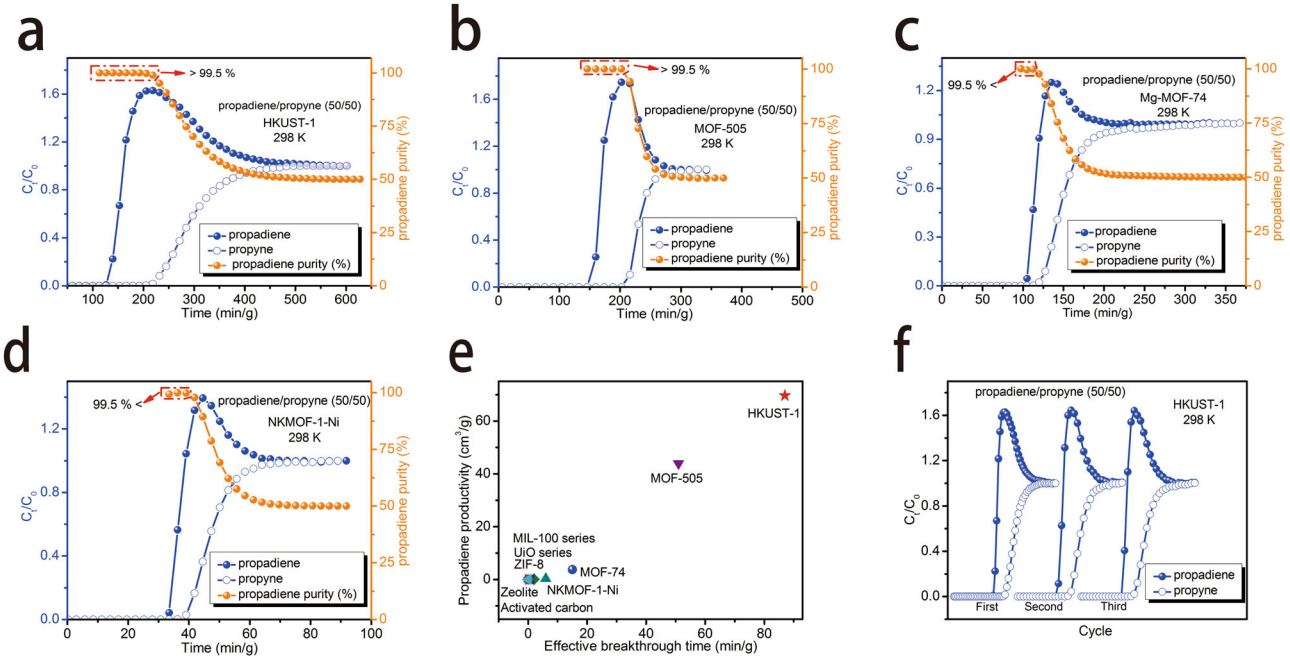

Fig. 4 Experimental breakthrough curves of the MOFs with OMSs for propyne/propadiene (50/50, v/v) separation at 298 K. a HKUST-1. **b** MOF-505. **c** Mg-MOF-74. **d** NKMOF-1-Ni. **e** Comparing productivity of propadiene for corresponding breakthrough experiments in the adsorbent library. **f** Cycling tests of HKUST-1 for propyne/propadiene mixture (gas velocity: 2.0 mL/min).

strong functional sites, including SIFSIX-2-Cu-i, SIFSIX-3-Ni, UTSA-200, and ZU-62, produced propadiene with lower purity (<95%, Supplementary Fig. 8d–g). Type-III MOFs without strong binding sites (UiO-66, UiO-67, and ZIF-8) were ineffective (Supplementary Fig. 8h–j). Overall, the hierarchy of separation performance was as follows: type-I MOFs with OMSs > type-II MOFs with strong functional sites > type-III MOFs without strong binding sites. The hierarchy of retention time for MOFs with OMSs was determined to be HKUST-1 > MOF-505 > MOF-74 > NKMOF-1-Ni » MIL-100-Cr, MIL-100-Fe, and MIL-101-Cr. HKUST-1 and MOF-505 possessed the best separation performance (Fig. 4 and Supplementary Fig. 8). Propadiene production of HKUST-1 and MOF-505 from the outlet effluent for a given cycle was calculated to be 69.6 and 43.9 cm^3/g, far exceeding that observed in Mg-MOF-74 (3.75 cm^3/g) and other materials (Fig. 4e). HKUST-1 is the benchmark material for separating propyne/propadiens as it exhibited the highest productivity of pure propadiene (>99.5%) via a one-step separation process. In order to gain insight into the mechanism, we systematically explored the equilibrium and kinetic adsorption behavior of gas molecules through further experimental studies and modeling.

Single-component equilibrium adsorption isotherms. Single-component equilibrium adsorption isotherms can directly show the adsorptive capacity of porous materials and provide indicators of sorbent-sorbate binding and separation selectivity. Propyne and propadiene equilibrium adsorption isotherms were measured at 273, 298, 308, and 318 K (Supplementary Figs. 9, 12–15). Type-III MOFs without strong binding sites possessed high adsorption capacity for both propyne and propadiene (Supplementary Fig. 9). However, they showed little difference in the adsorption profiles of propyne and propadiene over the pressure range tested. In the low-pressure area, the adsorption isotherms of propyne and propadiene overlapped, consistent with the dynamic breakthrough tests (Supplementary Fig. 8h–j). Type-II MOFs with electrostatic sites also showed similar adsorption behavior for propyne and propadiene, especially SIFSIX-3-Ni and UTSA-200 with isotherms overlapping from 0.1 to 1 bar, after reaching adsorption saturation at <0.1 bar. It was difficult to compare adsorption behavior at low pressure by a linear diagram (Supplementary Fig. 9) so we resorted to a logarithmic plot (Fig. 5 and Supplementary Fig. 10) which revealed similar sorption performance throughout the pressure range tested. Supplementary Fig. 9h, j reveal that SIFSIX-2-Cu-i and ZU-62 adsorb almost the same amount of propyne as propadiene, consistent with the relatively poor separation observed in our breakthrough experiments (Supplementary Fig. 8d and Supplementary Fig. 8f). Interestingly, although SIFSIX-3-Ni and UTSA-200 exhibited almost overlapping adsorption isotherms for propyne and propadiene from 0.1 to 1 bar, they exhibited preferential adsorption for propyne at 0.1 bar. However, they did not show strong separation performance in breakthrough experiments. As shown in Fig. 5, Type-I microporous MOFs with OMSs adsorbed propyne over propadiene throughout the pressure range tested, correlating with the breakthrough experiments detailed above (Fig. 4).

Isosteric heat of adsorption (Q_{st}) values reflect the affinity of a sorbent for a sorbate and are an indicator of thermodynamically driven separation. Type-I microporous MOFs with OMSs could be classified into two categories: (i) HKUST-1 and MOF-505 with cage-based molecule trap structure (Supplementary Fig. 11); (ii) Mg-MOF-74 and NKMOF-1-Ni with the regular one-dimensional channel. Their Q_{st} were evaluated by the Clausius–Clapeyron equation through fitting the adsorption isotherm using dual-site Langmuir (DSL) model and dual-site Langmuir–Freundlich (DSLF) model equation (Supplementary Figs. 12–15). The initial Q_{st} values for propyne and propadiene for HKUST-1, MOF-505, Mg-MOF-74, and NKMOF-1-Ni were 42 and 40, 78 and 58, 53 and 46, 65 and 54 kJ mol^{-1}, respectively (Supplementary Fig. 16). Q_{st} towards propyne was higher than that of propadiene for all optimized MOFs with OMSs. Massively Parallel MC (MPMC) theoretical calculations also indicated that the binding affinity for propyne was stronger than that for propadiene[47].

Ideal adsorbed solution theory (IAST) selectivity can be used to estimate thermodynamic separation performance. The selectivity

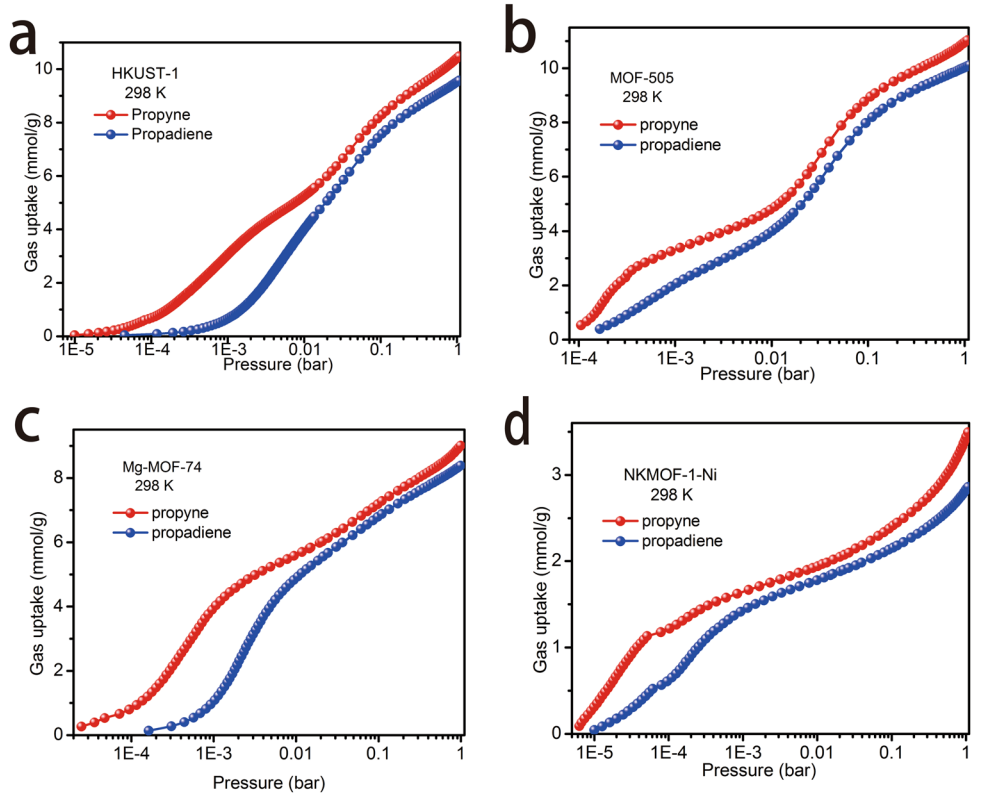

Fig. 5 Propyne and propadiene equilibrium adsorption isotherms of the selected MOF materials at 298 K. a HKUST-1. **b** MOF-505. **c** Mg-MOF-74. **d** NKMOF-1-Ni.

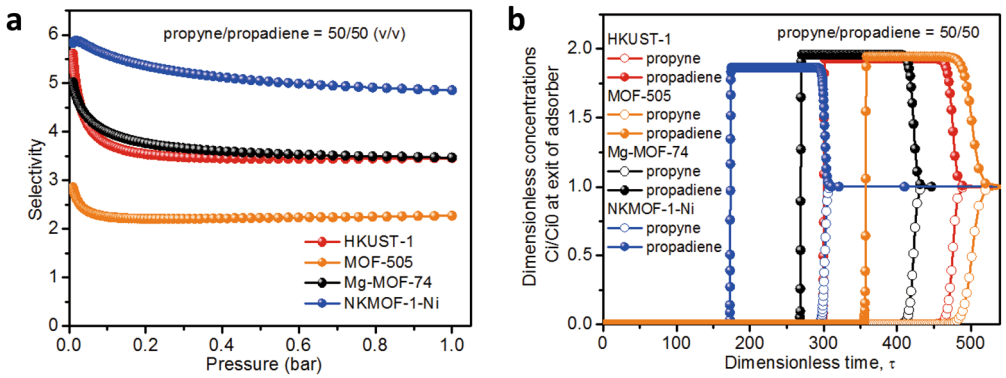

Fig. 6 IAST adsorption selectivities and simulation breakthrough curves for separation of propyne/propadiene for 50/50 (*v*/*v*) at 298 K. a IAST adsorption selectivities. **b** Simulation breakthrough curves.

of microporous MOFs with OMSs was calculated using IAST through fitting gas isotherm at 298 K by the DSL and DSLF equation (Supplementary Figs. 12–15). Considering the context of industrial separations, we calculated based on a propyne/propadiene (50/50, v/v) mixture at 298 K (Fig. 6a). NKMOF-1-Ni exhibited the highest selectivity of 6.0 with a selectivity > 4.8 across the pressure range. The selectivities of HKUST-1 and Mg-MOF-74 were slightly lower than NKMOF-1-Ni in the low-pressure area (<0.01 bar) and tended to be consistent with each other under the remaining pressure range (0.01–1 bar). These selectivity results indicate that microporous MOFs with OMSs materials should possess good separation performance.

In order to further evaluate separation performance, transient breakthrough simulations were conducted for propyne/propadiene feed mixtures (50/50, v/v) at 298 K and 1 bar using the methodology described in earlier publications[46]. Fig. 3b showed the outlet concentrations of propyne exiting in the fixed bed of HKUST-1, MOF-505, Mg-MOF-74, and NKMOF-1-Ni as a function of the dimensionless time, τ, for propyne/propadiene mixture. Although the IAST selectivity of NKMOF-1-Ni was the highest, the τ break value for NKMOF-1-Ni was not the highest, possibly attributing to its lowest uptake capacity for propyne. The simulated dynamic breakthrough results are related to adsorption selectivity, uptake capacity, and crystal density, etc. The hierarchy of the τ break values in the MOFs with OMSs is HKUST-1 > Mg-MOF-74 > MOF-505 > NKMOF-1-Ni. HKUST-1, MOF-505, Mg-MOF-74, and NKMOF-1-Ni demonstrated efficient and similar separation performance for propyne/propadiene (50/50, v/v) mixture.

Molecular simulation. For the purpose of gaining insight into the nature of the binding sites and energetics for propyne and

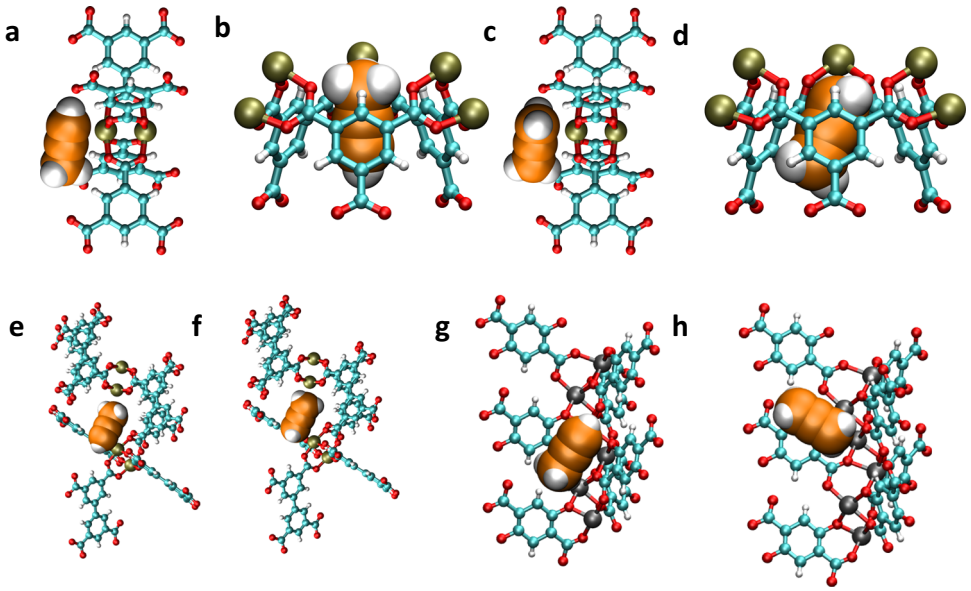

Fig. 7 Perspective views of a portion of the crystal structure of HKUST-1, MOF-505, and Mg-MOF-74, showing the optimized position of propyne and propadiene molecules. a OMSs units of HKUST-1 for propyne. **b** Tetrahedral cages units of HKUST-1 for propyne. **c** OMSs units of HKUST-1 for propadiene. **d** Tetrahedral cages units of HKUST-1 for propadiene. **e** OMSs units of MOF-505 for propyne. **f** OMSs units of MOF-505 for propadiene. **g** OMSs units of Mg-MOF-74 for propyne. **h** OMSs units of Mg-MOF-74 for propadiene. Atom colors: C(MOF) = cyan, C(propene) = orange, H = white, N = blue, O = red, Cu = oliver green, Mg = sliver.

propadiene in microporous MOFs with OMSs, we conducted classical Monte Carlo (MC) simulations (details are provided in Supplementary Notes 5). These simulations revealed that propyne and propadiene adsorb at two main binding sites in HKUST-1: (a) the Cu OMSs and (2) between tetrahedral cages. These are denoted as sites I and II, respectively (Figs. 7a–d). Calculation of the averaged classical potential energy for propyne and propadiene adsorbed at the site I in HKUST-1 afforded values of −54.15 and −50.74 kJ mol^{-1}, respectively (Supplementary Table 6). Notably, there are strong electrostatic and polarizable interactions between the positively charged Cu^{2+} ions of the copper paddlewheels and the unsaturated C atoms of the adsorbate molecules. The region between the tetrahedral cages is also favorable for propyne and propadiene, mainly due to strong π–π interactions between the aromatic rings of BTC linkers and the adsorbates. The averaged classical potential energy for propyne and propadiene adsorbed at site II in HKUST-1 were calculated to be −47.37 and −48.85 kJ mol^{-1}, respectively (Supplementary Table 6). The potential energy for propadiene at site II is slightly higher than that for propyne, presumably because it can make more contacts with the framework within this region due to having two π bonds positioned over three atoms (compared to two π bonds centered on two atoms in propyne). In general, the calculated potential energies for propyne and propadiene about both sites in HKUST-1 are comparable in magnitude to the Q_{st} values for the respective adsorbates (Supplementary Fig. 16a). Figure 7e, f shows the most favorable binding site for propyne and propadiene, respectively, in MOF-505 as determined through classical MC simulations. As with HKUST-1, both adsorbates bind to Cu^{2+} ions of the $[Cu_2(O_2CR)_4]$ units. The averaged classical potential energies for propyne and propadiene about the OMSs were calculated to be −89.17 and −43.19 kJ mol^{-1}, respectively (Supplementary Table 6). These values are comparable to the initial Qst values calculated for MOF-505 (Supplementary Fig. 16b). The potential energy for propyne is much greater than that for propadiene presumably because its longer length (6.51 vs. 6.13 Å, Fig. 1b) allows for simultaneous interaction between the Cu^{2+} ions of adjacent copper paddlewheels. In Mg-MOF-74, the exposed Mg^{2+} ions are preferential binding sites for propyne and propadiene (Fig. 7g, h). Similar to the Cu^{2+} binding sites in HKUST-1 and MOF-505, favorable interactions occur between positively charged Mg^{2+} ions and the negatively charged unsaturated C atoms of the adsorbate molecules. The averaged classical potential energy for propyne localized at this site is greater than that for propadiene (−78.46 and −60.62 kJ mol^{-1}, Supplementary Table 6). The calculated potential energy difference between propyne and propadiene in Mg-MOF-74 is similar to the difference in the initial Q_{st} values for both adsorbates (Supplementary Fig. 16c). It is known from our previous reports that NKMOF-1-Ni has a stronger affinity for propyne than propadiene[46]. Moreover, compared with HKUST-1 and MOF-505, Mg-MOF-74 and NKMOF-1-Ni have similar simulated breakthrough separation effects (Fig. 6b). But the results of the dynamic breakthrough experiments (Fig. 4) were less than satisfactory as the retained time of Mg-MOF-74 and NKMOF-1-Ni is much less than that of HKUST-1 and MOF-505. These results suggest that co-adorption or lack thereof may play a key role in the separation process.

Kinetic adsorption study. Considering the difference between the actual and the simulated breakthrough experiments, we measured the kinetic adsorption behavior of HKUST-1, MOF-505, Mg-MOF-74, and NKMOF-1-Ni (Fig. 8 and Supplementary Fig. S17). The adsorption rates of propyne in HKUST-1 and MOF-505, which comprised OMSs and microporous cage-based molecule trap structures, were observed to be faster than that of propadiene (Fig. 8a, b). However, for Mg-MOF-74 and NKMOF-1-Ni, which comprised OMSs and smooth one-dimensional channels, the kinetic adsorption curves of propyne and propadiene almost overlapped and crossed without noticeable selection difference (Supplementary Fig. 17a, b). The dynamic adsorption differences may be linked to cage-based molecule traps. HKUST-1 and MOF-505 are comprised of two kinds of cages with different sizes and shapes (Supplementary Fig. 11). In this way, the diffusion rate of different gas molecules in the process of adsorption will be affected by the cage windows, thus explaining

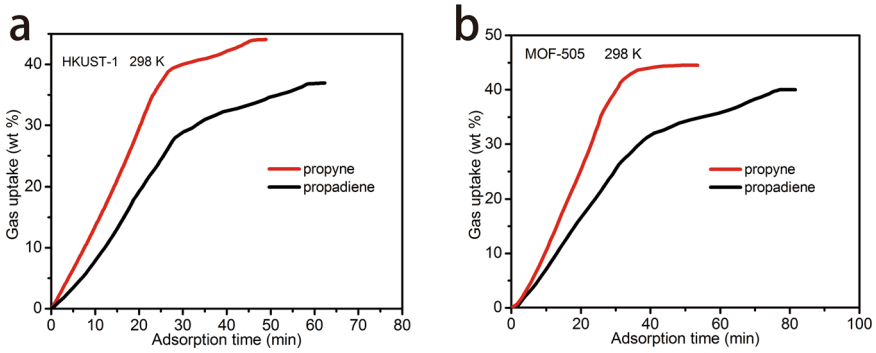

Fig. 8 Gravimetric propyne and propadiene sorption kinetics at 298 K. a HKUST-1. **b** MOF-505.

the diffusion rate of propyne vs. propadiene. For Mg-MOF-74 and NKMOF-1-Ni, which are comprised of open one-dimensional channels, gas molecules can freely diffuse in the channels. Moreover, whereas both propyne and propadiene strongly with OMSs in the channels of Mg-MOF-74 and NKMOF-1-Ni, their adsorption kinetics were similar. HKUST-1 and MOF-505 both exhibited benchmark separation performance for propyne/propadiene thanks to the synergy between kinetics and thermodynamics.

In summary, our study emphasizes the importance of both kinetics and thermodynamics with respect to the separation performance of propadiene vs. propyne. Dynamic gas mixture breakthrough experiments revealed that MOFs with OMSs and cage-based molecule traps exhibited such synergy to afford benchmark separation performance (propadiene production up to 69.6 cm^3/g, purity > 99.5%) whereas traditional porous materials such as activated carbon and zeolites showed no separation effect. Our study offers a design principle for sorbent selection along with a screening protocol that might be broadly applied for sorbent evaluation.

Methods

Preparation of MOF materials and characterization. All samples were synthesized according to Supplementary Method 2. PXRD test was conducted using microcrystalline samples on a Rigaku Ultima IV diffractometer (40 kV, 40 mA, Cu Kα1, $2\lambda = 1.5418$ Å). The measured parameter included a scan speed of 2 (°)/min, a step size of 0.02 (°). All MOFs samples were tested by ASAP 2020 PLUS Analyzer (Micromeritics) with Dewar (liquid N_2) and a homemade intelligent temperature control system (0–80 °C). The SEM images were obtained on HITACHI SU3500.

Breakthrough experiment. The breakthrough experiments were performed at a flow rate of 2 mL/min (298 K, 1.01 bar) for the propyne/propadiene (50/50, v/v) mixture. The MOF powder was packed into Φ 4 × 150 mm stainless steel column and activated by blowing pure helium (He). The column stacking density and column voidages of all samples tested were controlled in a similar condition. The breakthrough set-up consisted of two same fixed-bed stainless steel columns. One was used as a test sample and the other as a blank control to stabilize the gas flow. Both columns were housed in a temperature control system. The flow rates of all gases were regulated by mass flow controllers. The composition of the efflux gas of the test sample column was monitored by gas chromatography (Shimadzu, GC 2030, FID-Flame Ionization Detector, detection limit 100 ppb).

The propadiene productivity (q) was calculated by integration of the breakthrough curves $f(t)$. The purity of propadiene is higher or equal to a threshold value during the integration interval from $t1$ to $t2$

$$q = \frac{C_i(\text{propadiene})}{C_i(\text{propyne}) + C_i(\text{propadiene})} \times \left(\int_{t2}^{t1} f(t)dt \right)$$

Kinetic adsorption isotherm test. The kinetic adsorption behavior of HKUST-1, MOF-505, Mg-MOF-74, and NKMOF-1-Ni was performed on thermogravimetric analysis Instruments (Q50). During the test, we controlled the gas flow rate of propyne and propadiene to be 20 cm^3/min. The data was collected in the High-Resolution Dynamic mode with a sensitivity of 1.0, a resolution of 4.0, and the weight changes during propyne and propadiene gas adsorption step were monitored under the isothermal condition at 25 °C (298 K).

Q_{st}, IAST and transient breakthrough simulation calculation. The Q_{st} was determined from the unary isotherm by use of the Clausius–Clapeyron equation. IAST calculations were carried out for the following mixture 50/50 propyne/propadiene mixture at 298 K. Transient breakthrough simulations were carried out for 50/50 propyne/propadiene feed mixture at 298 K and 100 kPa.

Data availability

The authors declare that the data supporting the findings of this study are available within the article and its Supplementary Information.

Received: 28 May 2021; Accepted: 10 September 2021;
Published online: 01 October 2021

References

1. Roberts, J. D. & Sharts, C. M. Allene. *Org. React.* **12**, 23 (1962).
2. Williams, J. K. & Sharkey, W. H. Chemistry of cyclobutanes. III. synthesis of unsaturated four-membered ring hydrocarbons. *J. Am. Chem. Soc.* **81**, 4269–4272 (1959).
3. Roberts, D. W. On the mechanism of thermal 2+2 cycloaddition reactions involving fluoro-olefins. *Tetrahedron* **41**, 5529–5542 (1985).
4. Benson, R. E. & Lindsey, R. V. Jr Chemistry of allene. I. cyclopolymerization. synthesis and chemistry of 1, 2, 4- and 1, 3, 5-trimethylenecyclohexane and 1, 3, 5, 7-tetramethylenecycloöctane. *J. Am. Chem. Soc.* **81**, 4247–4250 (1959).
5. Lledó, A., Pla-Quintana, A. & Roglans, A. Allenes, versatile unsaturated motifs in transition-metal-catalysed [2+2+2] cycloaddition reactions. *Chem. Soc. Rev.* **45**, 2010–2023 (2016).
6. Liu, R. Y., Zhou, Y., Yang, Y. & Buchwald, S. L. Enantioselective allylation using allene, a petroleum cracking byproduct. *J. Am. Chem. Soc.* **141**, 2251–2256 (2019).
7. Sparks, W. J., Rosen, R. & Frolich, P. K. Dimerisation of petroleum hydrocarbons. *Trans. Faraday Soc.* **35**, 1040–1052 (1939).
8. Jones, E. R. H., Shaw, B. L. & Whiting, M. C. Researches on acetylenic compounds. Part XLVIII. The prototropic rearrangements of some diacetylenic dicarboxylic acids. *J. Am. Chem. Soc.* **76**, 3212–3217 (1954).
9. Crabbé, P., Nassim, B. & Robert-Lopes, M. T. One-step homologation of acetylenes to allenes: 4-hydroxynona-1, 2-diene: 1, 2-nonadien-4-ol. *Org. Synth.* **63**, 203–203 (2003).
10. Yoshikai, N. & Nakamura, E. Mechanisms of nucleophilic organocopper (I) reactions. *Chem. Rev.* **112**, 2339–2372 (2012).
11. Alfke, G., Irion, W. W. & Neuwirth, O. S. Refining, oil. In *Ullmann's Encyclopedia of Industrial Chemistry*. (Wiley-VCH, Weinheim, 2007).
12. Buckl, K. Propyne. In *Ullmann's Encyclopedia of Industrial Chemistry*. (ed. Buckl, K.) (Wiley-VCH: Weinheim, 2011).
13. Li, H. et al. Flow asymmetric propargylation: development of continuous processes for the preparation of a chiral β-amino alcohol. *Angew. Chem. Int. Ed.* **56**, 9425–9429 (2017).
14. Groome, N. M. et al. Carbophilic 3-component cascades: access to complex bioactive cyclopropyl diindolylmethanes. *Chem. Eur. J.* **19**, 2180–2184 (2013).
15. Elboray, E. E., Gao, C. & Grigg, R. Skeletal diversity via Pd(0) catalysed three-component cascades of allene and halides or triflates with protected hydroxylamines and formamide. *Tetrahedron* **68**, 3103–3111 (2012).

16. Ahmar, M., Barieux, J.-J., Cazes, B. & Gore, J. Carbopalladation of allenic hydrocarbons: a new way to functionalized styrenes and 1,3-butadienes. *Tetrahedron* **43**, 513–526 (1987).
17. Kitagawa, S. Porous materials and age of the gas. *Angew. Chem. Int. Ed.* **54**, 10686–10687 (2015).
18. Lowell, S., Shields, J. E., Thomas, M. A. & Thommes. M. *Characterization of Porous Solids and Powders: Surface Area, Pore Size and Density*. (Springer, New York, 2006).
19. Peng, Y. L. et al. Robust ultramicroporous metal-organic frameworks with benchmark affinity for acetylene. *Angew. Chem. Int. Ed.* **130**, 11137–11141 (2018).
20. Ding, Q. et al. Separation of propylene and propane with a microporous metal-organic framework via equilibrium-kinetic synergetic effect. *AIChE J.* **67**, e17094 (2020).
21. Lan, T. et al. Opportunities and critical factors of porous metal-organic frameworks for industrial light olefins separation. *Mater. Chem. Front.* **4**, 1954–1984 (2020).
22. Lin, R. B., Xiang, S., Zhou, W. & Chen, B. Microporous metal-organic framework materials for gas separation. *Chemistry* **6**, 337–363 (2019).
23. Nangia, A. K. & Desiraju, G. R. Crystal engineering: an outlook for the future. *Angew. Chem. Int. Ed.* **58**, 4100–4107 (2019).
24. Schoedel, A. et al. The asc trinodal platform: two-step assembly of triangular, tetrahedral, and trigonal-prismatic molecular building blocks. *Angew. Chem. Int. Ed.* **125**, 2974–2977 (2013).
25. Guillerm, V. et al. A supermolecular building approach for the design and construction of metal-organic frameworks. *Chem. Soc. Rev.* **43**, 6141–6172 (2014).
26. Sholl, D. S. & Lively, R. P. Defects in metal-organic frameworks: callenge or opportunity? *J. Phys. Chem. Lett.* **6**, 3437–3444 (2015).
27. Gascon, C. A., Grande, J., Kapteijn, F. & Rodrigues, A. E. Propane/propylene separation with Li-exchanged Zeolite 13X. *Chem. Eng. J.* **160**, 207–214 (2010).
28. Kim, M. B. & Thallapally, P. K. Effective CH4/N2 separation using NU-1000 at high pressures. *J. Coord. Chem.* **74**, 216–225 (2021).
29. Liao, P. Q., Zhang, W. X., Zhang, J. P. & Chen, X. M. Efficient purification of ethene by an ethane-trapping metal-organic framework. *Nat. Commun.* **6**, 1–9 (2015).
30. Li, L. et al. Ethane/ethylene separation in a metal-organic framework with iron-peroxo sites. *Science* **362**, 443–446 (2018).
31. Zeng, H. et al. Cage-interconnected metal-organic framework with tailored apertures for efficient C2H6/C2H4 separation under humid conditions. *J. Am. Chem. Soc.* **141**, 20390–20396 (2019).
32. Bloch, E. D. et al. Hydrocarbon separations in a metal-organic framework with open Iron (II) coordination sites. *Science* **335**, 1606–1610 (2012).
33. Yang, H. et al. Pore-space-partition-enabled exceptional ethane uptake and ethane-selective ethane-ethylene separation. *J. Am. Chem. Soc.* **142**, 2222–2227 (2020).
34. Matsuda, R. et al. Highly controlled acetylene accommodation in a metal-organic microporous material. *Nature* **436**, 238–241 (2005).
35. Yang, S. et al. Supramolecular binding and separation of hydrocarbons within a functionalized porous metal-organic framework. *Nat. Chem.* **7**, 121–129 (2014).
36. Cui, X. et al. Pore chemistry and size control in hybrid porous materials for acetylene capture from ethylene. *Science* **353**, 141–144 (2016).
37. Lin, R. B. et al. Optimized separation of acetylene from carbon dioxide and ethylene in a microporous material. *J. Am. Chem. Soc.* **139**, 8022–8028 (2017).
38. Gao, J. et al. Mixed metal-organic framework with multiple binding sites for efficient C2H2/CO2 separation. *Angew. Chem. Int. Ed.* **59**, 4396–4400 (2020).
39. Li, B. & Chen, B. Fine-tuning porous metal-organic frameworks for gas separations at will. *Chemistry* **1**, 669–671 (2016).
40. Yang, L. et al. A single-molecule propyne trap: highly efficient removal of propyne from propylene with anion-pillared ultramicroporous materials. *Adv. Mater.* **30**, 1705374 (2018).
41. Wang, H., Liu, Y. & Li, J. Designer metal-organic frameworks for size-exclusion-based hydrocarbon separations: progress and challenges. *Adv. Mater.* **32**, 2002603 (2020).
42. He, C. et al. Modification of the pore environment in UiO-type metal-organic framework toward boosting the separation of propane/propylene. *Chem. Eng. J.* **403**, 126428 (2021).
43. Ferreira, A. F. et al. Suitability of Cu-BTC extrudates for propane-propylene separation by adsorption processes. *Chem. Eng. J.* **167**, 1–12 (2011).
44. Meyer, V., Sutter, D. H. & Vogelsanger, B. Molecular g-tensor, molecular magnetic susceptibility anisotropy, and molecular electric quadrupole moment tensor of allene from a rotational zeeman effect study of 1, 1-dideuteroallene. *J. Mol. Spectrosc.* **148**, 436–446 (1991).
45. Haynes, W. M. (Ed.). *CRC Handbook of Chemistry and Physics* (CRC Press, 2014).
46. Peng, Y. L. et al. Robust microporous metal-organic frameworks for highly efficient and simultaneous removal of propyne and propadiene from propylene. *Angew. Chem. Int. Ed.* **58**, 10209–10214 (2019).
47. Xiang, S., Zhou, W., Gallegos, J. M., Liu, Y. & Chen, B. Exceptionally high acetylene uptake in a microporous metal-organic framework with open metal sites. *J. Am. Chem. Soc.* **131**, 12415–12419 (2009).
48. McKinstry, C., Cussen, E. J., Fletcher, A. J., Patwardhan, S. V. & Sefcik, J. Scalable continuous production of high quality HKUST-1 via conventional and microwave heating. *Chem. Eng. J.* **326**, 570–577 (2017).

Acknowledgements

This work is supported by financial support from the National Natural Science Foundation of China (21971126), Science Foundation Ireland (SFI Awards 13/RP/B2549 and 16/IA/4624), National Science Foundation (Award No. DMR-1607989), the Major Research Instrumentation Program (Award No. CHE-1531590), XSEDE grant (No. TG-DMR090028), National Key Research and Development Program of China (2020YFA0907300). We would like to thank Research Computing at the University of South Florida, and High-Performance Computing at North Carolina State University and thank Dr. Shanelle Suepaul for her assistance with making pictures and Ananya Jain for preliminary efforts to parametrize MOF-505 for simulations.

Author contributions

Z.Z. and Y.-L.P. conceived the project. Z.Z. and M.Z. supervised the project. Y.-L.P. designed the experiments, Y.-L.P. and T.W. performed the synthetic experimental work. Y.-L.P. performed the majority of the structural characterization and data analysis. Y.-L.P. and T.W. collected and analyzed gas sorption data. K.A.F., R.K., T.P., B.S., and W.L did the modeling study. Y.-L.P., Z.Z., and M.Z. drafted the paper. C.J., C.D., Y.Z., Y.C., and P.C. edited the paper. All authors discussed and revised the paper.

Competing interests

The authors declare no competing interests.

Additional information

Supplementary information The online version contains supplementary material available at https://doi.org/10.1038/s41467-021-25980-y.

Correspondence and requests for materials should be addressed to Zhenjie Zhang.

Peer review information *Nature Communications* thanks Feng Luo and the other, anonymous, reviewer(s) for their contribution to the peer review of this work.

Reprints and permission information is available at http://www.nature.com/reprints

Publisher's note Springer Nature remains neutral with regard to jurisdictional claims in published maps and institutional affiliations.

Supplementary Information for

Efficient Propyne/Propadiene Separation by Microporous Crystalline Physiadsorbents

Yun-Lei Peng, Ting Wang, Chaonan Jin, Cheng-Hua Deng, Yanming Zhao,Wansheng Liu, Katherine A. Forrest, Rajamani Krishna, Yao Chen, Tony Pham, Brian Space, Peng Cheng, Michael J. Zaworotko, Zhenjie Zhang*
*Correspondence to: zhangzhenjie@nankai.edu.cn (Z. Z.)

Supplementary Methods:

1. **General Materials**

1,3,5-Tricarboxybenzene (98%, innochem), 2,5-Dihydroxy-1,4-benzenedicarbo--xylic acid (H_4DOBDC) (98%, innochem), Biphenyl-3,3',5,5'-tetracarboxylic Acid (99%, innochem), Pyrazine (99%, innochem), 1,4-Benzenedicarboxylic acid (99%, Macklin), Biphenyl-4,4'-dicarboxylic acid (97%, Heowns,Tianjin), 4,4'-azopyridine (95+%, HUAWEIRUIKE), 2,3-dichloropyrazine (98%, Bide Pharmatech Ltd), 4-(2-pyridin-4-ylethynyl), Pyridine (98%, HUAWEIRUIKE), 1-Methylimidazole (99%, aladdin), $Cu(NO_3)_2{\cdot}3H_2O$ (Analytical reagent, Gerhardite), $ZrCl_4$ (99.9%, Aladdin), $Zn(NO_3){\cdot}6H_2O$ (99.9%, Heowns,Tianjin), $(NH_4)_2{\cdot}SiF_6$ (Analytical reagent, Greagent), $CuSiF_6$ (Analytical reagent, Greagent), $Ni(BF_4)_2{\cdot}6H_2O$ (Energy chemical), Sodium hydroxide (NaOH, 97%, Aladdin), Sodium hydrosulfide (NaHS, LiDeShi), Copper(II) perchlorate hexahydrate ($Cu(ClO_4)_2{\cdot}6H_2O$, 98%, Strem Chemical, Inc.), Niobium Oxide (Nb_2O_5, 99.9%, Macklin), Nickel tetrafluoroborate hexahydrate ($Ni(BF_4)_2{\cdot}6H_2O$, 99%, Aldrich), Chromic nitrate ($Cr(NO_3)_3$, 99%, Macklin), Chromium sesquioxide (Cr_2O_3, 99%, Macklin), Iron powder (99.95%, Aladdin), N,N-dimethyl-Formamide

(DMF), Ethanol,, Methanol, Acetonitrile, Ether, and Acetone were purchased and used without further purification. He, N_2, propyne ($CH_3C{\equiv}CH$), and propadiene ($CH_2{=}C{=}CH_2$), CO_2, were purchased from AIR LIQUIDE. The powder X-ray diffraction data were obtained on Rikagu ULTIMA IV.

2. **MOFs Synthesis**

Synthesis of HKUST-1: HKUST-1 was synthesized based on the previous method.[1] $Cu(NO_3)\cdot 2.5H_2O$ (6.0 g) was dissolved into 250 mL deionized water. It was followed by the addition of 1,3,5-Tricarboxybenzene (4.0 g) in a 250 mL of solvent consisting of equal parts of ethanol and deionized water and mixed thoroughly until it was completely dissolved. The resultant solution mixture was transferred into a 250 mL teflon-lined stainless steel autoclave. It was kept at 110 ℃ for 18 h in oven to yield small crystals. Then the autoclave was cooled down to room temperature naturally and the blue crystals were isolated by filtration. The suspension was washed with the mixture of deionized water and ethanol several times and dried.

Synthesis of MOF-505: MOF-505 was synthesized based on the previous method.[2] A solid mixture of Biphenyl-3,3',5,5'-tetracarboxylic Acid (H_4bptc; 25 mg, 0.076 mmol) and $Cu(NO_3)_2\cdot(H_2O)_{2.5}$ (52 mg, 0.22 mmol) was added 5ml mixture solvent (DMF/ethanol/H_2O 3/3/2 (v/v/v)) in 20 mL scintillation vials. The reaction vials were capped tightly with Teflon-lined caps and placed in an oven at 65℃ for 24 hours. Then the gave green, block shaped Crystals was yield.

Synthesis of Mg-MOF-74: Mg-MOF-74 was synthesized based on the previous method.[3] A solid mixture of H_4DOBDC (0.111 g, 0.559 mmol) and $Mg(NO_3)_2\cdot 6H_2O$

(0.475 g, 1.85 mmol) was added 50 ml mixture solvent (DMF/ethanol/water 15/1/1 (v/v/v)). The suspension was mixed and ultrasonicated until homogeneous. The reaction solution was then dispensed to five 20 mL scintillation vials. The reaction vials were capped tightly with Teflon-lined caps and placed in an oven at 125 °C for 20 hours. Then the samples were removed from the oven and allowed to cool to RT. The mother liquor was decanted from the yellow microcrystalline material and replaced with methanol (10 mL per vial). The yellow microcrystalline material was combined into one vial. The methanol was decanted and replenished four times over two days. The solvent was removed under vacuum at 250 °C over 10 hours, yielding the dark yellow microcrystalline, porous material.

Synthesis of NKMOF-1-Ni: NKMOF-1-Ni was synthesized based on the previous method.[4] CuI (0.2143 g, 1.125 mmol) was dissolved in acetonitrile (30 mL) by sonication. $Na[Ni(pdt)_2]\cdot 2H_2O$ (0.30 g, 0.75 mol) was dissolved in acetonitrile (200 mL) and bubbled with argon for 1 hour. Subsequently, CuI solution was dropwise added into $Na[Ni(pdt)_2]\cdot 2H_2O$ solution. After 2 hours, dark red powders of NKMOF-i-Ni were obtained by centrifugation.

Synthesis of MIL-100 (Cr, Fe): MIL-100 (Cr) was synthesized based on the previous method.[5] Metallic chromium (52 mg, 1 mmol) was dispersed into an aqueous solution of 5M hydrofluoric acid (0.4 mL, 2 mmol). After the addition of 1,3,5-benzene tricarboxylic acid (H_3BTC) (150 mg, 0.67 mmol) and H_2O (4.8 mL, $265 * 10^{-3}$mol), the mixture was heated in ahydrothermal bomb at a rate of 20 ℃/h to 220 ℃, kept at this temperature during 96 h, then cooled at a rate of 10 ℃/h to room temperature. The

resulting green powder was washed with deionized water and acetone and dried in air.

MIL-100 (Fe) was synthesized based on the previous method.[6] This solid was isolated as a polycrystalline powder from a reaction mixture of composition Fe/ H_3BTC /HF/HNO_3/H_2O (1.0/0.66/2.0/1.2/280) that was held at 150 ℃ in a Teflon-lined autoclave for 6 days with a initial heating ramp of 12 h and a final cooling ramp of 24 h. The pH remains acidic (<1) throughout the synthesis. The light-orange solid product was recovered by filtration and washed with deionized water. A treatment in hot deionised water (80 ℃) for 3 h was applied to decrease the amount of residual H_3BTC (typically, 1 g of MIL-100(Fe) in 350 ml of water) followed by drying at room temperature.

Synthesis of MIL-101 (Cr): MIL-101 (Cr) was synthesized based on the previous method.[7] A typical synthesis involves a solution containing chromium(III) nitrate $Cr(NO_3)_3 \cdot 9H_2O$ (400 mg, 1 mmol, 1 mmol of fluorhydric acid, 1,4-benzene dicarboxylic acid H_2BDC (164 mg, 1 mmol) in 4.8 ml H_2O (265 mmol); the mixture is introduced in a hydrothermal bomb which is put during 8h in an autoclave held at 220°C. A treatment in hot deionised water (80 ℃) for 3 h was applied to decrease the amount of residual H_3BTC followed by drying at room temperature.

Synthesis of SIFSIX-2-Cu-i: SIFSIX-2-Cu-i was synthesized based on the previous method.[8] A methanol solution of 1,2-bis(4-pyridyl)acetylene (dpa) (4 mL, 0.270 mmol) was stirred with an aqueous solution of $CuSiF_6$ (4 mL, 0.258 mmol) resulting in a purple precipitate, which was then heated at 85°C for 12 hrs.

Synthesis of SIFSIX-3-Ni: SIFSIX-3-Ni was synthesized based on the previous

method.[9] SIFISIX-3-Ni was synthesized by slurrying 870 mg (3 mmol) of $Ni(NO_3)_2$, 534 mg (3 mmol) of $(NH_4)_2SiF_6$ and 480 mg (6 mmol) of pyrazine in 4 mL of water for 2 days. The resulting suspension was filtered under vacuum and dried in air. This precursor was soaked in methanol for 1 day and then washed twice with two portions (ca. 10 mL) of methanol on a Buchner filter. After drying in air, the solid was heated at 140 ˚C for 1 day to obtain SIFSIX-3-Ni.

Synthesis of UTSA-200 (SIFSIX-14-Cu-i): UTSA-200 (SIFSIX-14-Cu-i) was synthesized based on the previous method.[10] A methanol solution (3 mL) of azpy (0.266 mmol) was mixed with an aqueous solution of $CuSiF_6$ (2.5 mL, 0.247 mmol) at 80°C resulting in a bright grey precipitate, which was then heated at 80°C for 15 min, additional 1 h at 50°C, and then at room temperature for 24 h.

Synthesis of ZU-62: ZU-62 was synthesized based on the previous method.[11] A preheated water solution (4.0 mL) of $CuNbOF_5$ (0.0730 g) were dropped into a preheated methanol solution (4.0mL) of 4, 4'-bipyridylacetylene (0.0515 g). Then the mixture was heated at 80 °C for 24 h. The obtained blue power was exchanged with methanol for a day.

Synthesis of UiO-66: UiO-66 was synthesized based on the previous method.[12] Standard synthesis of UiO-66 was performed by dissolving $ZrCl_4$ (0.053 g, 0.227 mmol) and 1,4-benzenedicarboxylic acid (H_2BDC) (0.034g, 0.227 mmol) in DMF (24.9 g, 340 mmol) at room temperature. The thus obtained mixture was sealed and placed in a pre-heated oven at 120 ˚C for 24 hours. Crystallization was carried out under static conditions. After cooling in air to room temperature the resulting solid was filtered,

repeatedly washed with DMF and dried at room temperature.

Synthesis of UiO-67: UiO-67 was synthesized based on the previous method.[12] Standard synthesis of UiO-67 was performed by dissolving $ZrCl_4$ (0.053 g, 0.227 mmol) and 1,4-benzenedicarboxylic acid (H_2BPDC) (0.227 mmol) in DMF (24.9 g, 340 mmol) at room temperature. The thus obtained mixture was sealed and placed in a pre-heated oven at 120 ˚C for 24 hours. Crystallization was carried out under static conditions. After cooling in air to room temperature the resulting solid was filtered, repeatedly washed with DMF and dried at room temperature.

Synthesis of ZIF-8: ZIF-8 was synthesized based on the previous method.[13] A solid mixture of zinc nitrate tetrahydrate $Zn(NO_3)_2 \cdot 4H_2O$ (0.210 g, 0.803 mmol) and 2-methylimidazole (H-MeIM) (0.060 g, 0.731 mmol) was dissolved in 18 mL DMF in a 20-mL vial. The vial was capped and heated at a rate of 5 ºC /min to 140 ºC in a programmable oven, held at this temperature for 24 h, then cooled at a rate of 0.4 ºC/min to room temperature. After removal of mother liquor from the mixture, chloroform (20 mL) was added to the vial. Colorless polyhedral crystals of the product were collected from the upper layer, washed with DMF (10 mL × 3) and dried in air (10 min).

Supplementary Notes:

Supplementary Note 1: Fitting of experimental data on pure component isotherm

The unary isotherm data for propyne and propadiene in HKUST-1 and Mg-MOF-74 (at 273 K and 298 K) were individually fitted with the dual-site Langmuir (DSL) model:

$$q = \frac{q_{sat,A} b_A p}{1 + b_A p} + \frac{q_{sat,B} b_B p}{1 + b_B p}$$ **Supplementary Equation 1**

The isotherm fit parameters for HKUST-1 are provided in Supplementary Table 2. The isotherm fit parameters for Mg-MOF-74 are provided in Supplementary Table 3.

The unary isotherm data for propyne and propadiene in MOF-505 (at 273 K and 298 K) and NKMOF-1-Ni (at 298 K and 318 K) were individually fitted with the dual-site Langmuir-Freundlich (DSLF) model:

$$q = \frac{q_{sat,A} b_A p^{V_a}}{1 + b_A p^{V_A}} + \frac{q_{sat,B} b_B p^{V_B}}{1 + b_B p^{V_B}}$$ **Supplementary Equation 2**

The isotherm fit parameters for MOF-505 are provided in Supplementary Table 4. The isotherm fit parameters for NKMOF-1-Ni are provided in Supplementary Table 5.

Supplementary Note 2: Isosteric heat of adsorption

The isosteric heat of adsorption was determined from the unary isotherm by use of the Clausius-Clapeyron equation:

$$Q_{st} = RT^2 \left(\frac{\partial \ln p}{\partial T} \right)_q$$ **Supplementary Equation 3**

These values were determined using the pure component isotherm fits using the DSL and DSLF equation (Supplementary Fig. 12-14). $\boldsymbol{Q_{st}}$ is the coverage dependent isosteric heat of adsorption and $\boldsymbol{R}$ is the universal gas constant.

Supplementary Note 3: IAST calculations of adsorption selectivity and uptake capacity

IAST calculations were carried out for the following mixture 50/50 propyne/propadiene mixture at 298 K. the adsorption selectivity is defined by:

$$S_{ads} = \frac{q_A / q_B}{y_A / y_B}$$ **Supplementary Equation 4**

Where the q_A, and q_B represent the molar loadings within the MOF that is in equilibrium with a bulk fluid mixture with mole fractions y_A, and y_B =1 - y_A. The molar loadings, also called gravimetric uptake capacities, are usually expressed with the units mol Kg^{-1}. The IAST calculations of propyne/propadiene adsorption selectivites taking the mole fractions y_A = 0.5 and y_B = 1 - y_A = 0.5 for a total pressure of 100 kPa and 298 K.

Supplementary Note 4: Transient breakthrough simulation

The performance of industrial fixed bed adsorbers is dictated by a combination of adsorption selectivity and uptake capacity. Transient breakthrough simulations were carried out for 50/50 propyne/propadiene feed mixture at 298 K and 100 kPa using the methodology described in earlier publications.[14-18] For the breakthrough simulations, the following parameter values were used: length of packed bed, L = 0.3 m; voidage of packed bed, ε = 0.4; superficial gas velocity at inlet, u = 0.04 m/s. The y-axis is the dimensionless concentrations of each component at the exit of the fixed bed, c_i / c_{i0}

normalized with respect to the inlet feed concentrations. The x-axis is the dimensionless time, $\tau = \frac{tu}{L\varepsilon}$, defined by dividing the actual time, *t*, by the characteristic time, $\frac{L\varepsilon}{u}$.

Notation

b	Langmuir-Freundlich parameter,
q	component molar loading of species i, mol kg^{-1}
q_{sat}	saturation loading, mol kg^{-1}
L	length of packed bed adsorber, m
t	time, s
T	absolute temperature, K
u	superficial gas velocity in packed bed, m s^{-1}

Greek letter

ε	voidage of packed bed, dimensionless
ν	Freundlich exponent, dimensionless
τ	time, dimensionless

Supplementary Note 5: Modeling Study

All parametrizations and simulations in HKUST-1 and MOF-505 were performed on the single X-ray crystallographic structure of the materials as published in references (CCDC 112954)[19] and (CCDC 257470),[20]]respectively. The polarizable force field that was developed for Mg-MOF-74 in previous work was used herein.[21]

All atoms of HKUST-1 and MOF-505 were treated with Lennard-Jones (LJ) parameters (ε and σ), point partial charges,[22] and point polarizabilities in order to model repulsion/dispersion, stationary electrostatic, and many-body polarization interactions, respectively. The LJ parameters for all atoms were taken from the Universal Force Field (UFF).[23] The partial charges for the chemically distinct atoms in both MOFs were determined through electronic structure calculations on different gas phase fragments that were selected from the crystal structure of the respective MOFs. These calculations were performed using the NWChem *ab initio* software with the 6-31G* basis set assigned to C, H, and O and the LANL2DZ ECP basis set assigned to Cu.[24-27] The exponential damping-type polarizability values for all C, H, and O atoms were taken from a carefully parametrized set provided by the work of van Duijnen and Swart.[28] The polarizability parameter for Cu^{2+} was calculated in previous work and used herein.[29]

Classical Monte Carlo (MC) simulations of propyne and propadiene adsorption were performed within the unit cell of HKUST-1, 2 × 2 × 1 supercell of MOF-505, and 1 × 1 × 4 supercell of Mg-MOF-74. All MOF atoms were kept fixed at their crystallographic positions. For each MOF, a spherical cut-off distance corresponding to half the shortest system cell dimension length was used for the simulations. Propyne and propadiene were modeled using polarizable potentials of the respective adsorbates that were developed previously.[30] The total potential energy of the MOF-adsorbate system was calculated through the sum of the repulsion / dispersion, stationary electrostatic, and many-body polarization energies. These were calculated using the

Lennard-Jones 12-6 potential,[22] partial charges with Ewald summation, [31,32] and a Thole-Applequist type model,[33-36] respectively. All MC simulations were performed using the Massively Parallel Monte Carlo (MPMC) code. [37,38]

In order to identify the global minimum for propyne and propadiene in HKUST-1, MOF-505, and Mg-MOF-74, simulated annealing (SA) calculations were performed for a single molecule of each adsorbate through a Canonical Monte Carlo (CMC) process in the considered system cell of the individual MOFs.[39] All SA calculations utilized an initial temperature of 500 K, and this temperature was scaled by a factor of 0.99999 after every 1.0×10^3 MC steps. The simulations continued until 1.0×10^6 MC steps were reached; at this point, the temperature of the system is below 10 K and the adsorbate is already localized in its energy minimum position in the MOF. For all three MOFs, the global minimum for propyne and propadiene was observed to be localization onto the open-metal sites. Additional SA calculations in HKUST-1 revealed that propyne and propadiene also settled into the tetrahedral cages, which represent the local minimum (i.e., secondary binding site) in the material.

Next, CMC simulations were performed for a single molecule of propyne and propadiene, individually, positioned at their global minimum in all three MOFs.[40] This was done in order to evaluate the averaged classical potential energy for both adsorbates about their energy minimum position in the respective materials. The CMC simulations were performed at a temperature of 298 K and a pressure of 0.10 atm. These simulations ran for a total of 1.0×10^6 MC steps to ensure reasonable ensemble averages for the total potential energy of the system. Similar CMC simulations were carried out for both

adsorbates initially positioned within the tetrahedral cage in HKUST-1. The averaged classical potential energies for propyne and propadiene localized about the favorable binding sites in HKUST-1, MOF-505, and Mg-MOF-74 are presented in Supplementary Table 6.

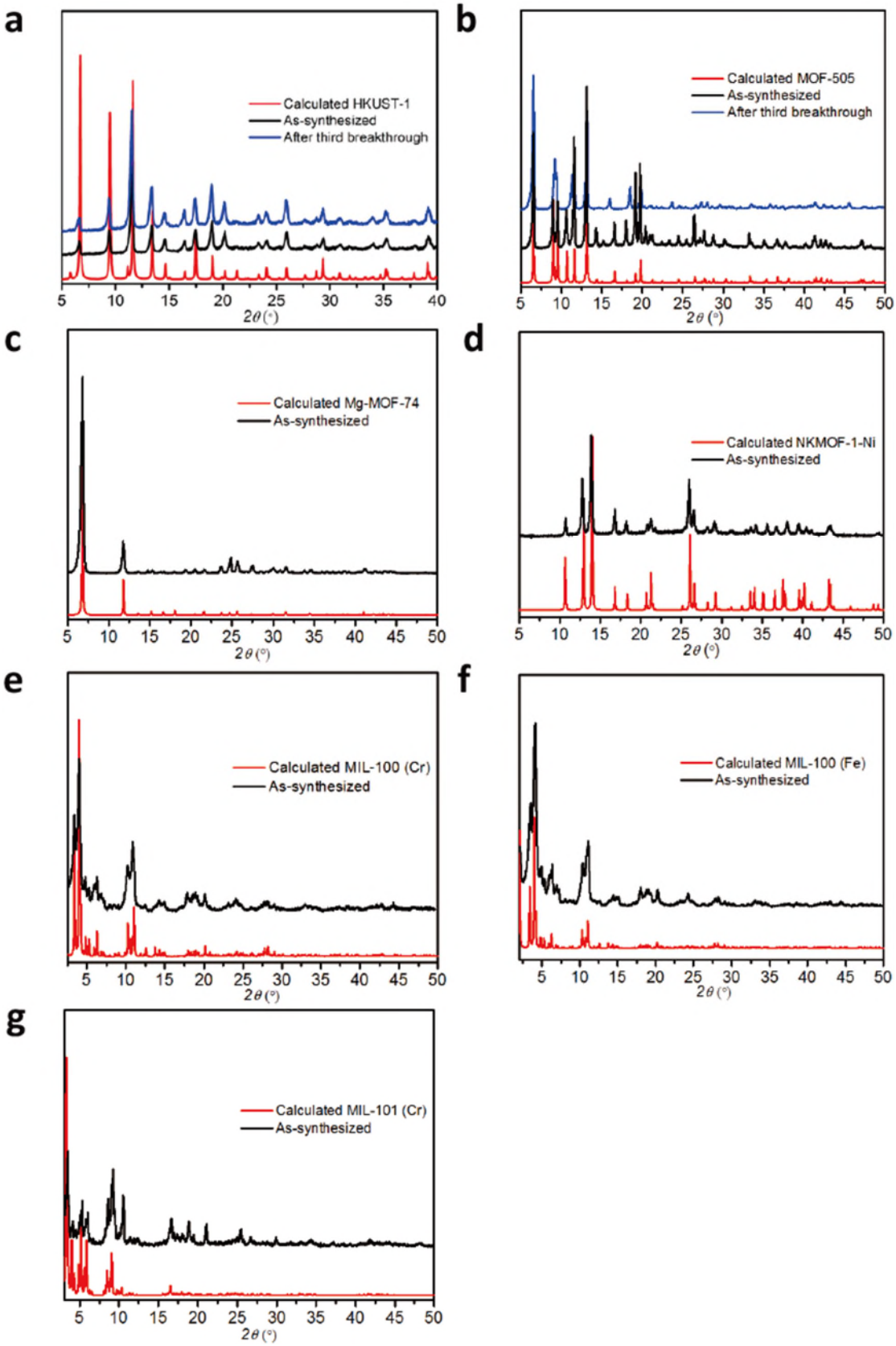

Supplementary Fig. 1 The PXRD patterns of the MOFs with open metal sites (OMSs). **a** HKUST-1. **b** MOF-505. **c** Mg-MOF-74. **d** NKMOF-1-Ni. **e** MIL-100(Cr). **f** MIL-100(Fe). **g** MIL-101.

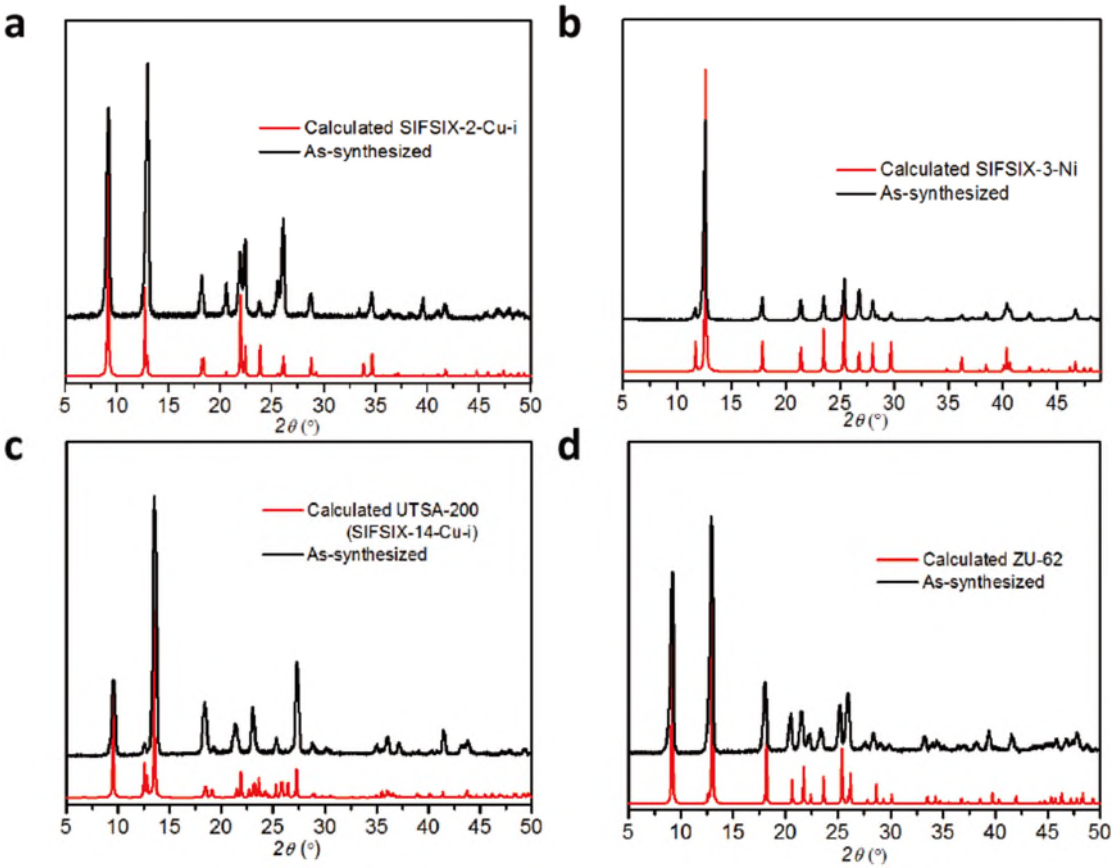

Supplementary Fig. 2 The PXRD patterns of the MOFs with strong binding sites. **a** SIFSIX-2-Cu-i. **b** SIFSIX-3-Ni. **c** UTSA-200. **d** ZU-62.

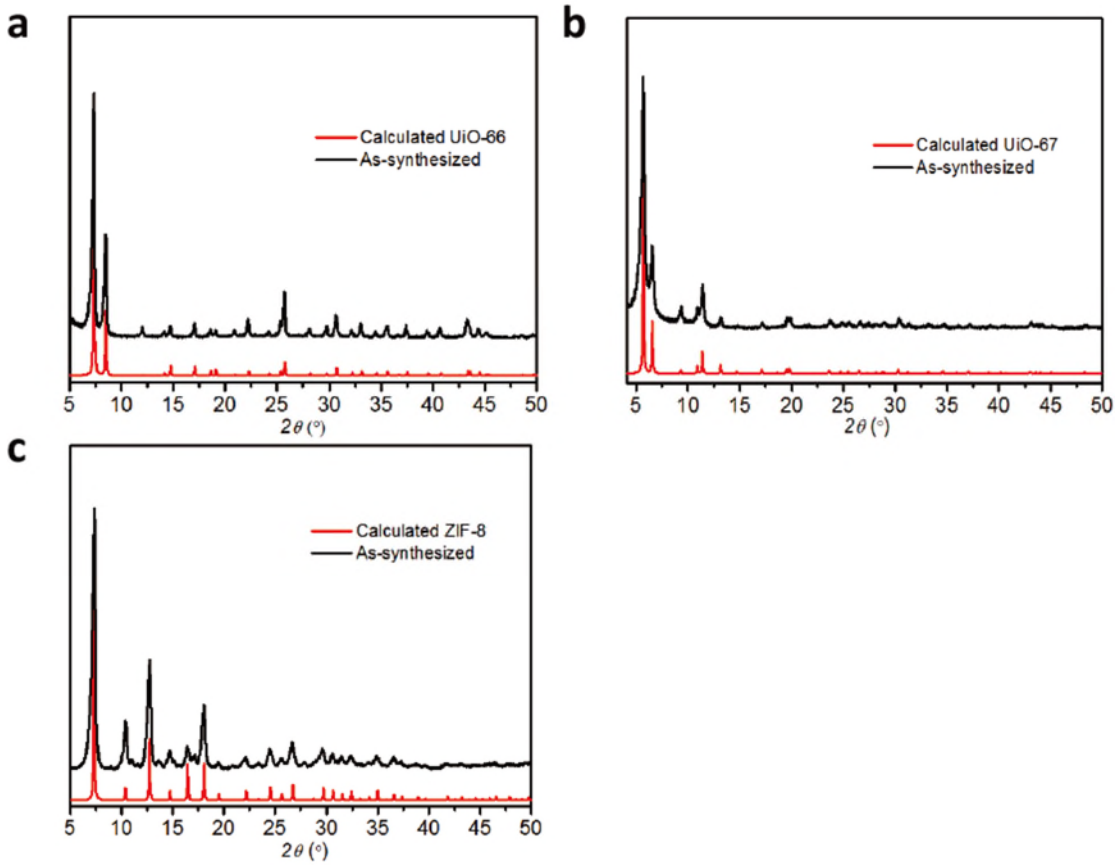

Supplementary Fig. 3 The PXRD patterns of the MOFs without strong binding sites. **a** UiO-66. **b** UiO-67. **c** ZIF-8.

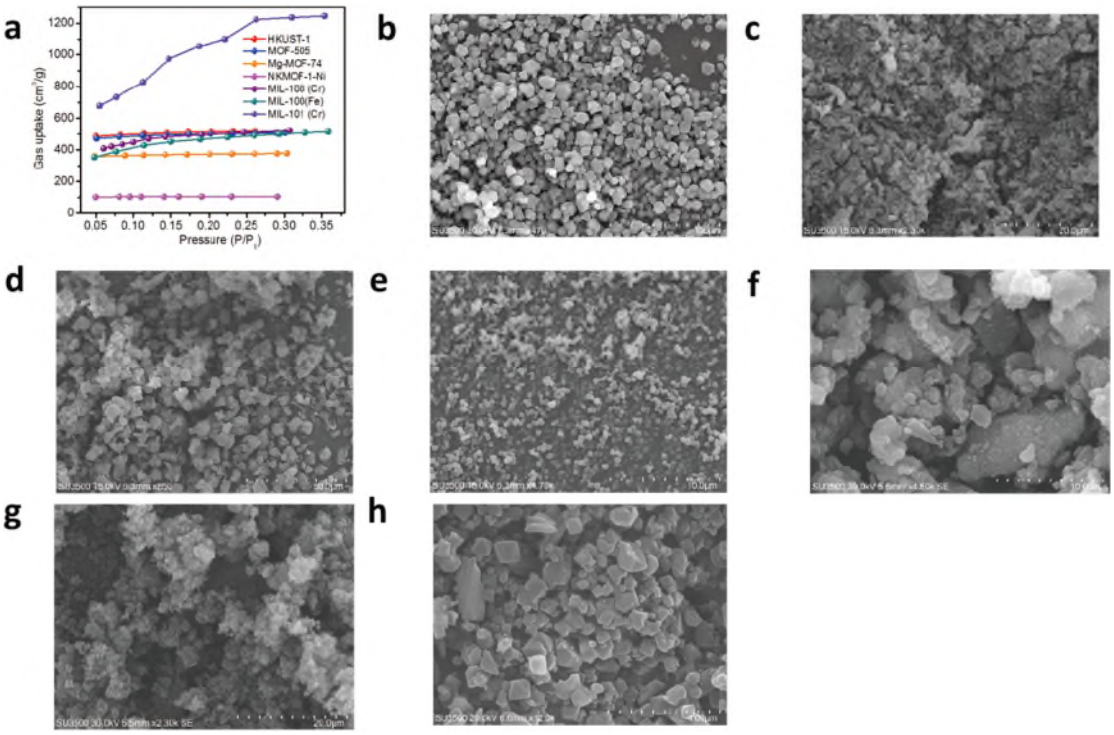

Supplementary Fig. 4 BET and SEM measurements for MOFs with open metal sites. **a** N_2 adsorption of MOFs with open metal sites at 77K. **b**-**h** The SEM images for HKUST-1, MOF-505, Mg-MOF-74, NKMOF-1-Ni, MIL-100(Cr), MIL-100(Fe) and MIL-101(Cr).

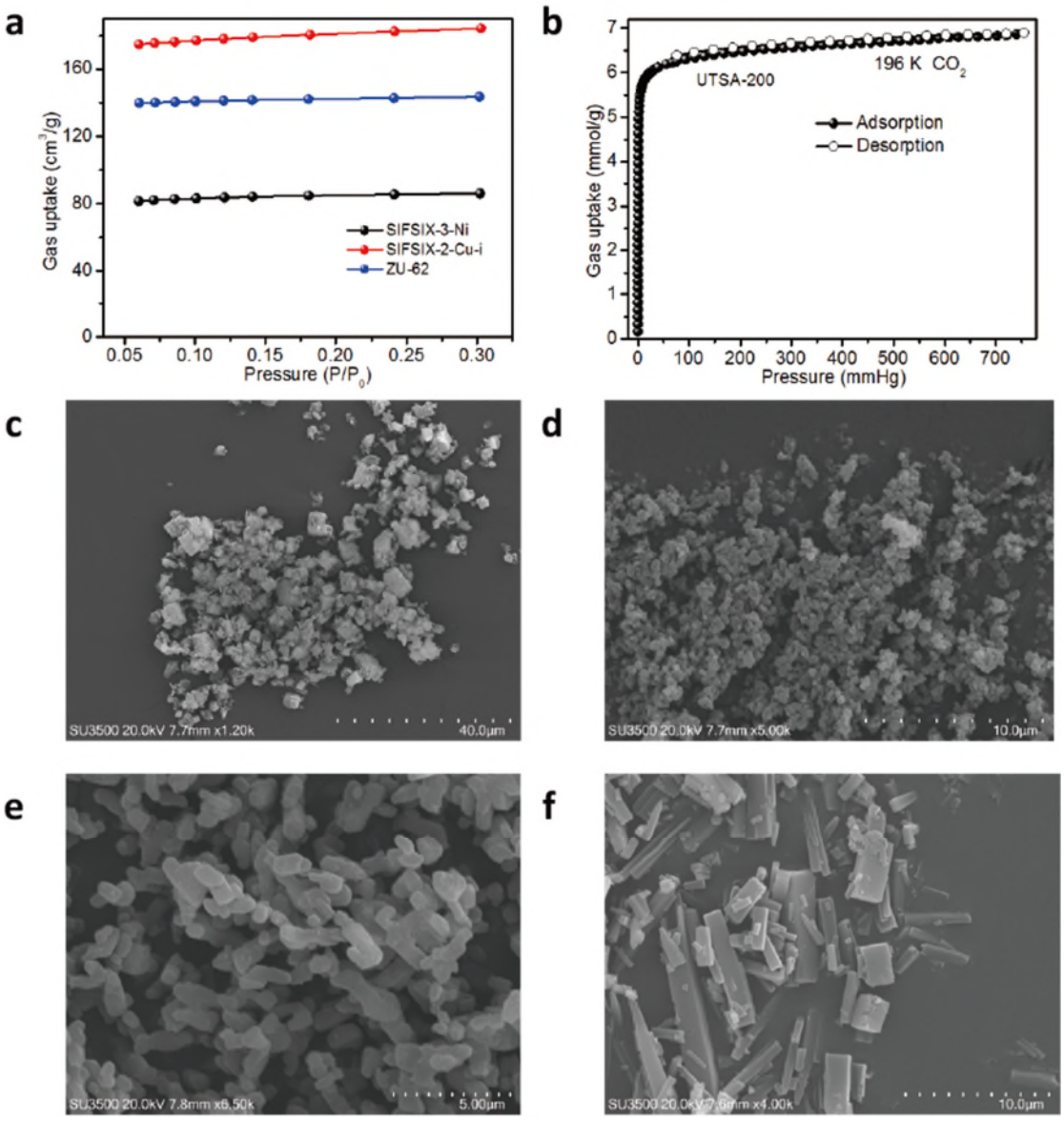

Supplementary Fig. 5 BET and SEM measurements for MOFs with strong binding sites. **a** N_2 adsorption of SIFSIX-3-Ni, SIFSIX-2-Cu-i and ZU-62 at 77K. **b** CO_2 adsorption of UTSA-200 at 196K. **c-f** The SEM images for SIFSIX-3-Ni, SIFSIX-2-Cu-i, ZU-62 and UTSA-200.

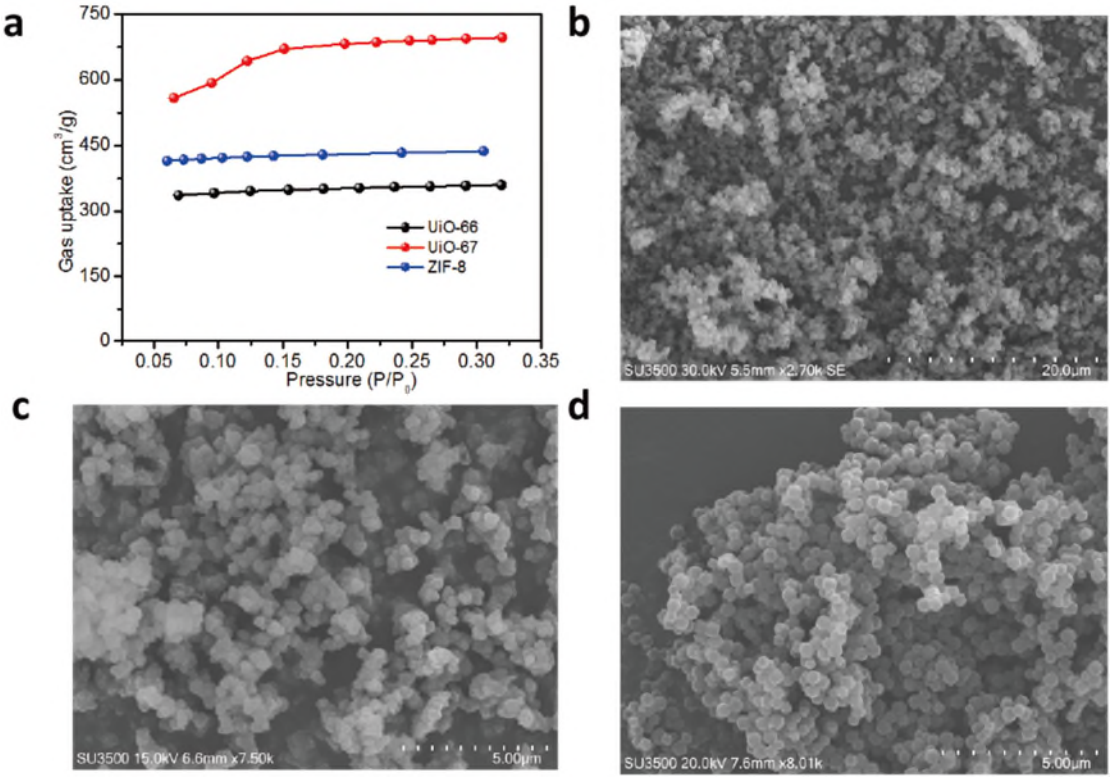

Supplementary Fig. 6 BET measurements for MOFs without strong binding sites. **a** N_2 adsorption of UiO-66, UiO-67 and ZIF-8 at 77K. **b-d** The SEM images for UiO-66, UiO-67 and ZIF-8.

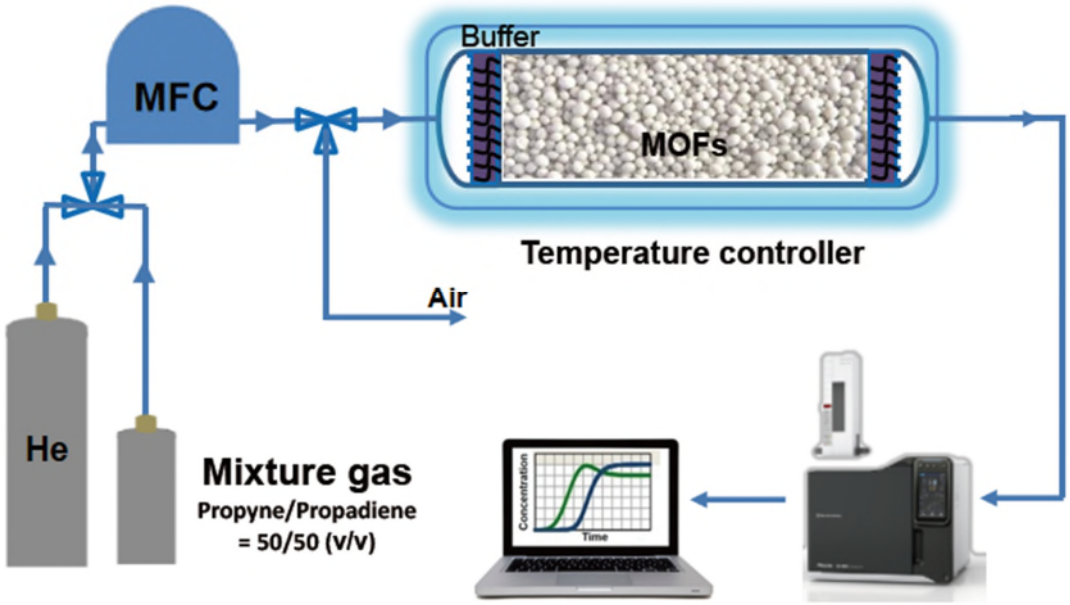

Supplementary Fig. 7 Breakthrough separation apparatus. (MFC= Mass Flow Controller)

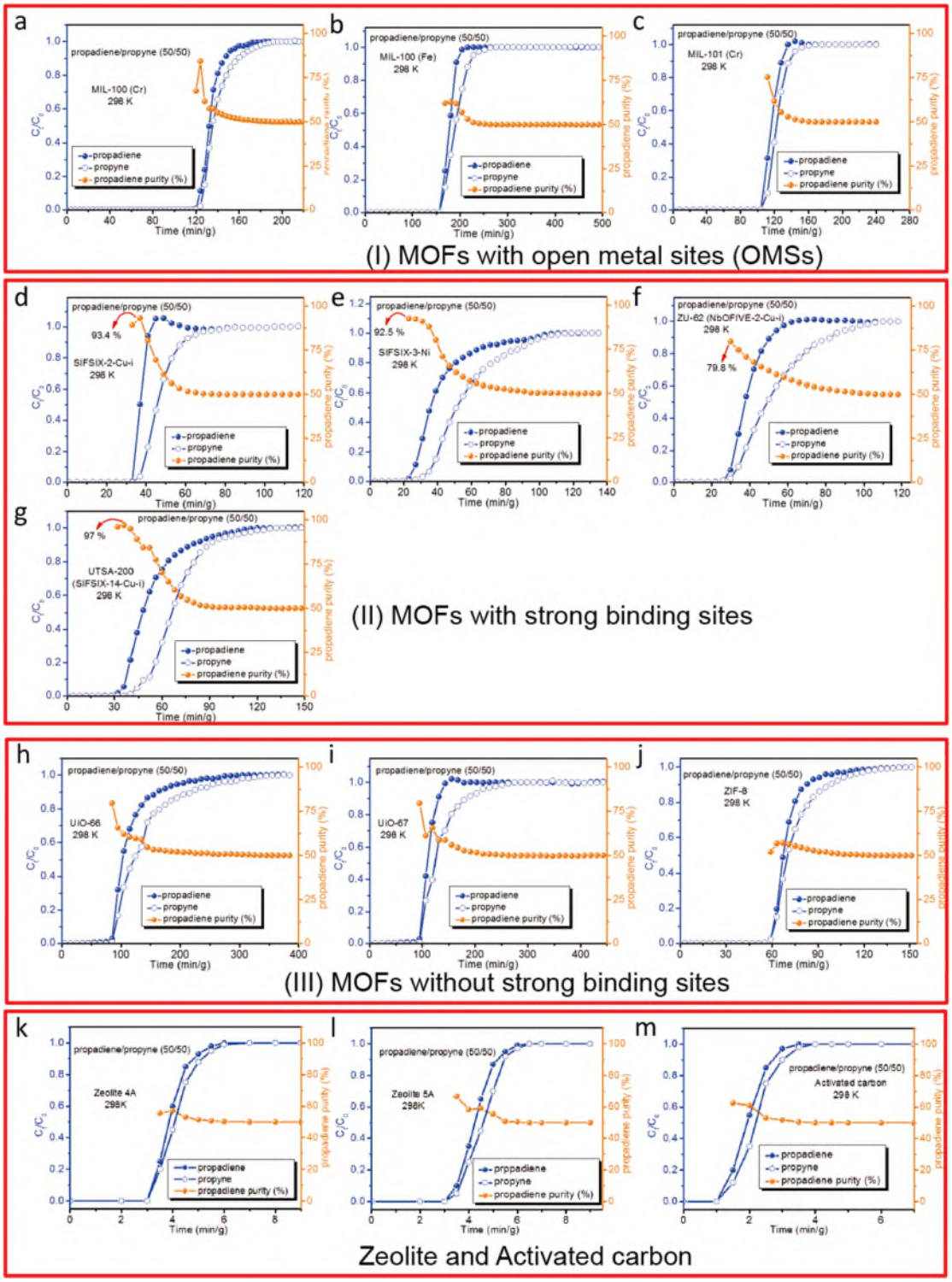

Supplementary Fig. 8 Experimental breakthrough curves of the selected MOF materials for propyne/propadiene (50/50, v/v) at 298 K. **a**, **b**, **c** MOFs with open metal sites (MIL-100(Cr), MIL-100 (Fe) and MIL-101 (Cr)). **d**, **e**, **f**, **g** MOFs with strong binding sites (SiF_6^{2-} and $NbOF_5^{2-}$) (SIFSIX-2-Cu-i, SIFSIX-3-Ni, ZU-62, and UTSA-200). **h**, **i**, **j** some MOFs without strong binding sites (UiO-66, UiO-67, and ZIF-8). **k** Zeolite 4A. **l** Zeolite 5A. **m** Activated carbon.

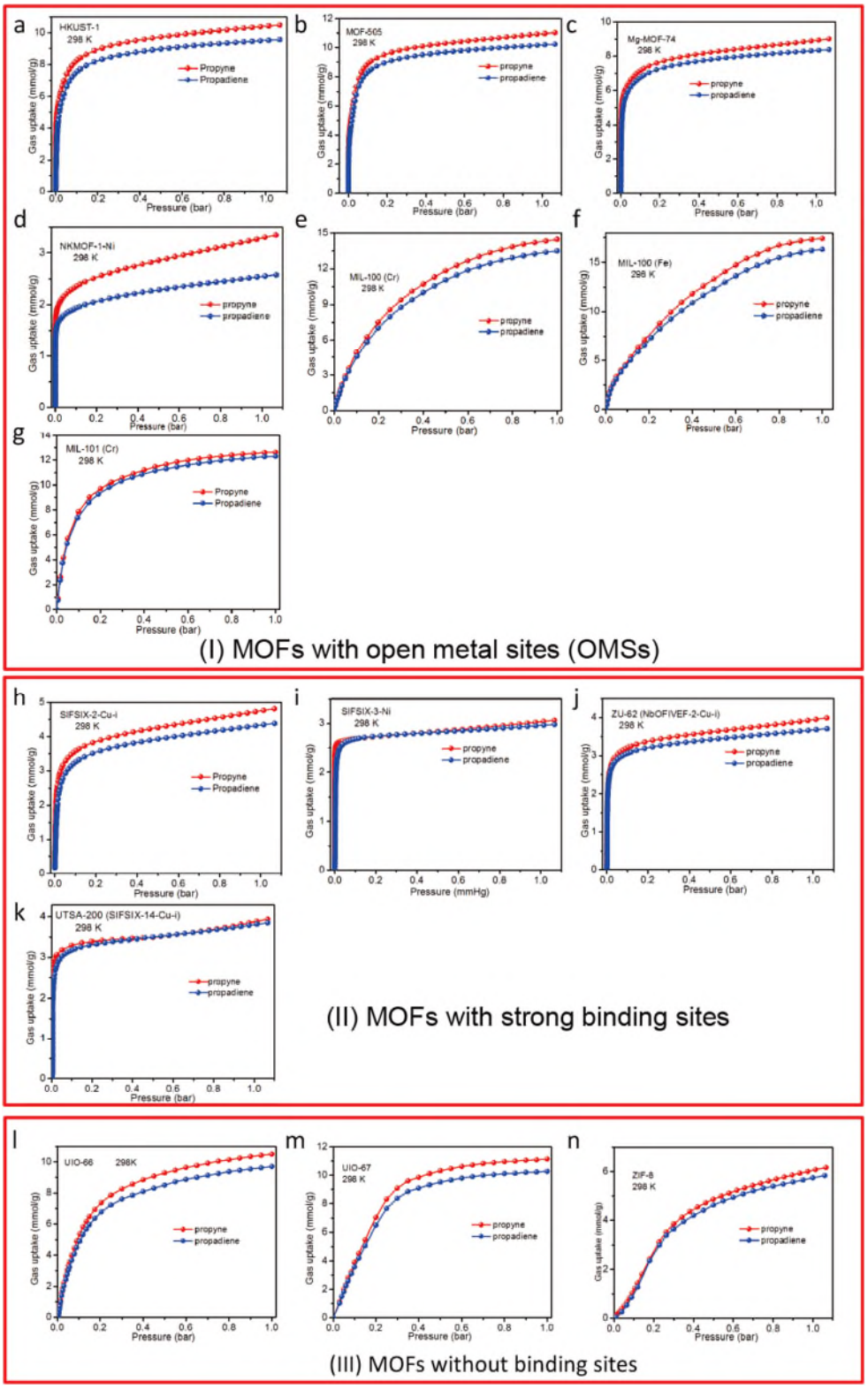

Supplementary Fig. 9 Experimental propyne (red) and propadiene (blue) adsorption isotherms of the selected MOF materials at 298 K. **a**, **b**, **c**, **d**, **e**, **f**, **g** MOFs with open metal sites (HKUST-1, MOF-505, Mg-MOF-74, NKMOF-1-Ni, MIL-100(Cr), MIL-100(Fe) and MIL-101(Cr)). **h**, **i**, **j, k** MOFs with strong binding sites (SiF_6^{2-} and $NbOF_5^{2-}$ sites) (SIFSIX-2-Cu-i, SIFSIX-3-Ni, ZU-62, and UTSA-200). **l**, **m, n** MOFs without binding sites (UiO-66, UiO-67 and ZIF-8).

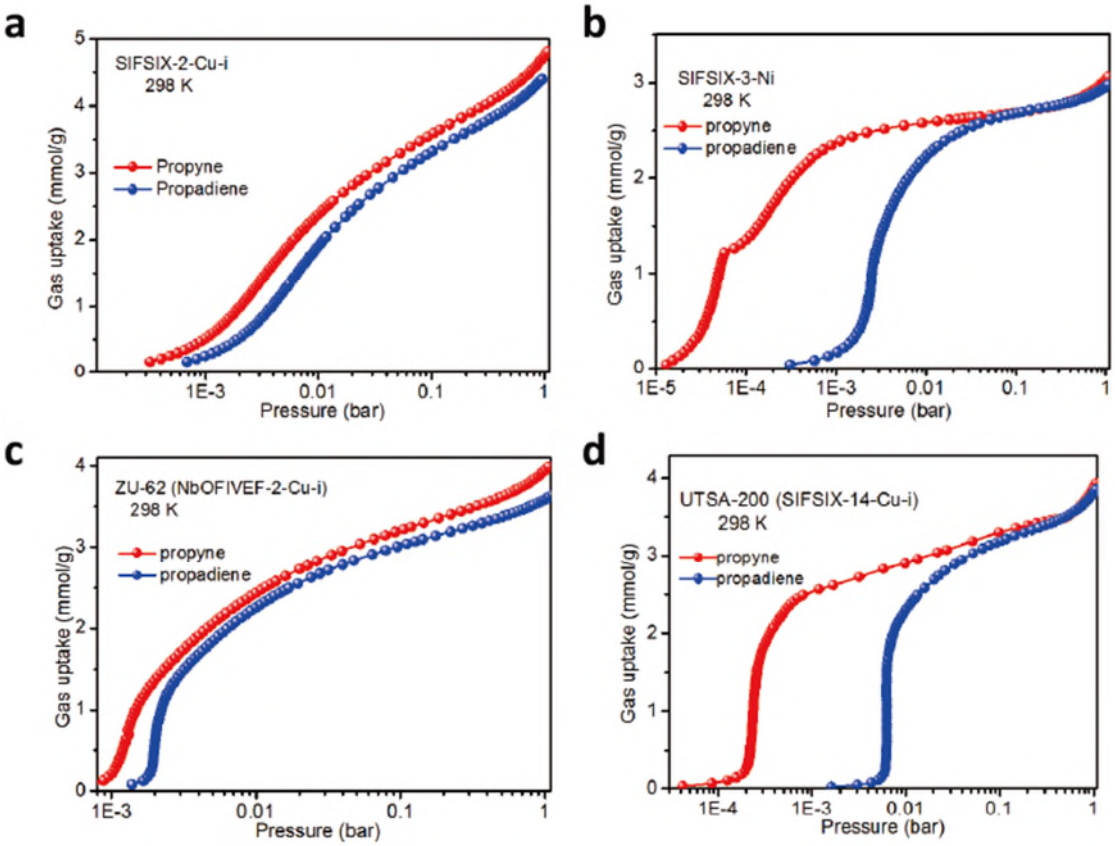

Supplementary Fig. 10 propyne (red) and propadiene (blue) equilibrium adsorption isotherms of MOFs with strong binding sites. **a** SIFSIX-2-Cu-i. **b** SIFSIX-3-Ni. **c** ZU-62. **d** UTSA-200.

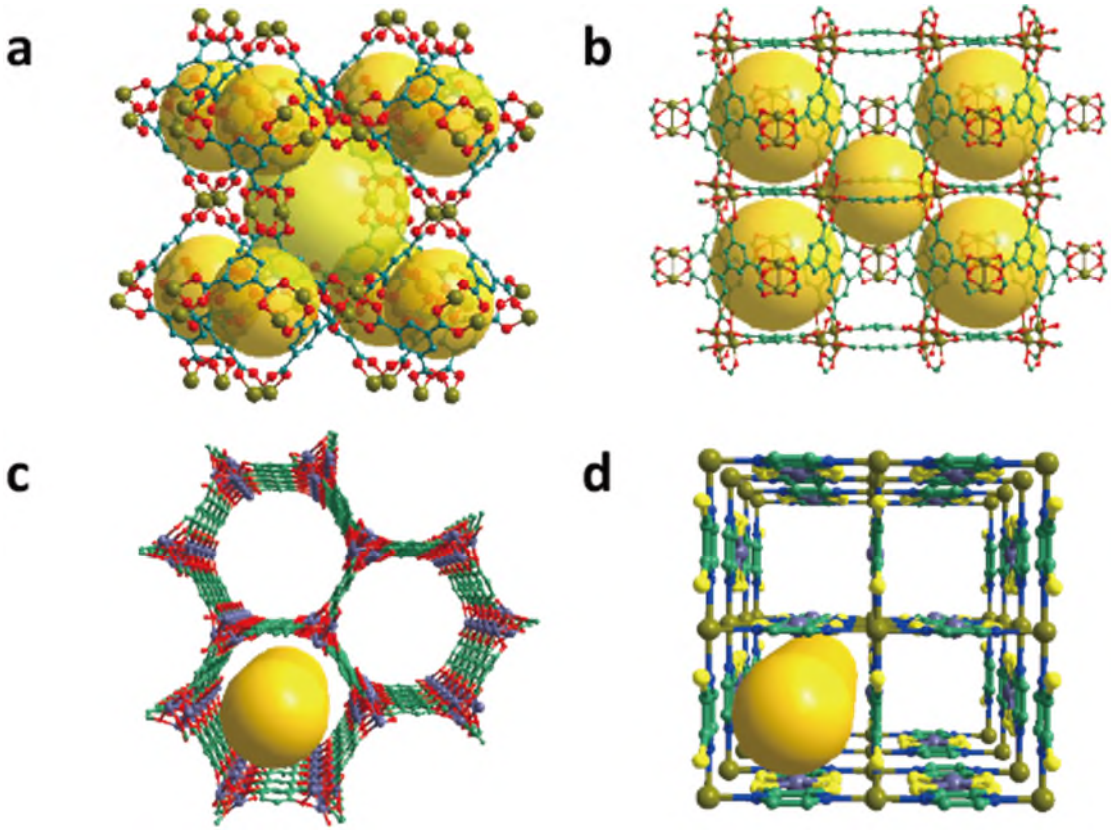

Supplementary Fig. 11 The schematic of microporous MOFs with OMSs. **a, b** HKUST-1 and MOF-505 with OMSs and cage-based structure. **c, d** Mg-MOF-74 and NKMOF-1-Ni with OMSs and smooth one-dimensional channels. Atom colors: C(MOF) = sea green, N = blue, O = red, Cu = dark yellow, Ni = sliver, Mg = blue gray.

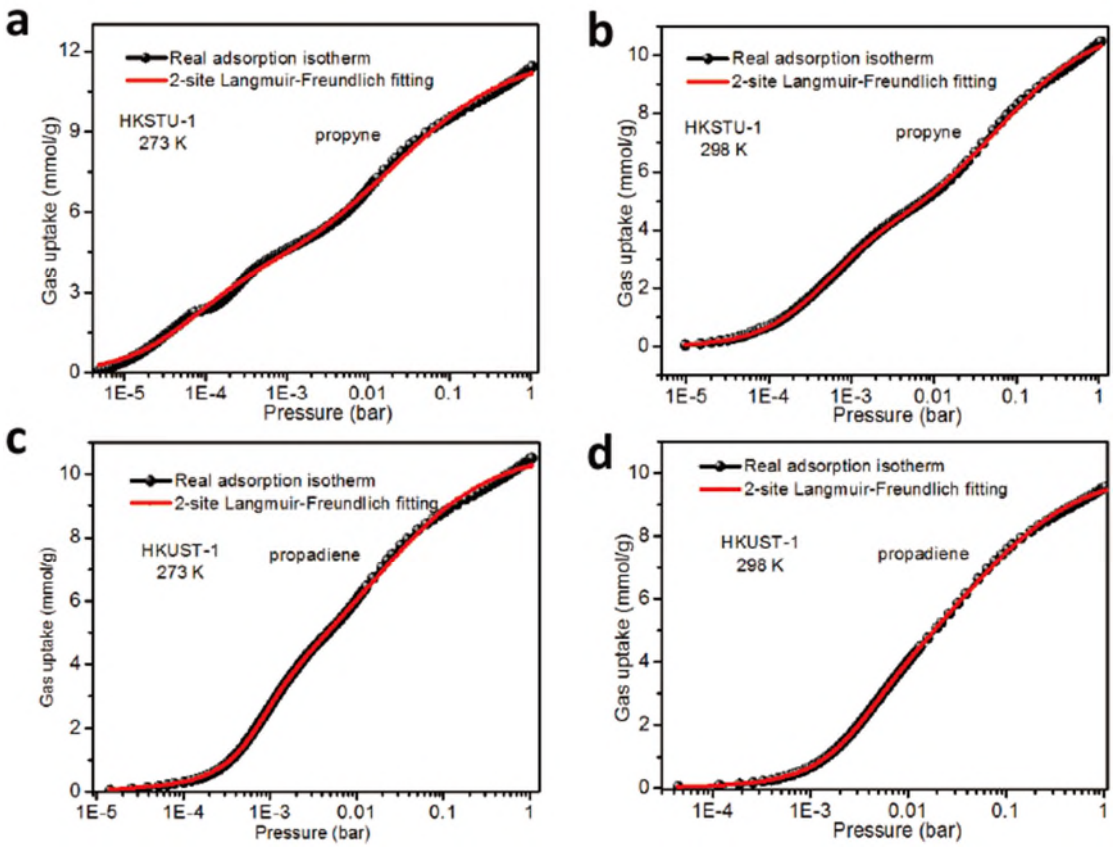

Supplementary Fig. 12 Dual-site Langmuir-Freundlich model fits of propyne and propadiene adsorption isotherms at 273 K and 298 K in HKUST-1. **a, b** propyne. **c, d** propadiene.

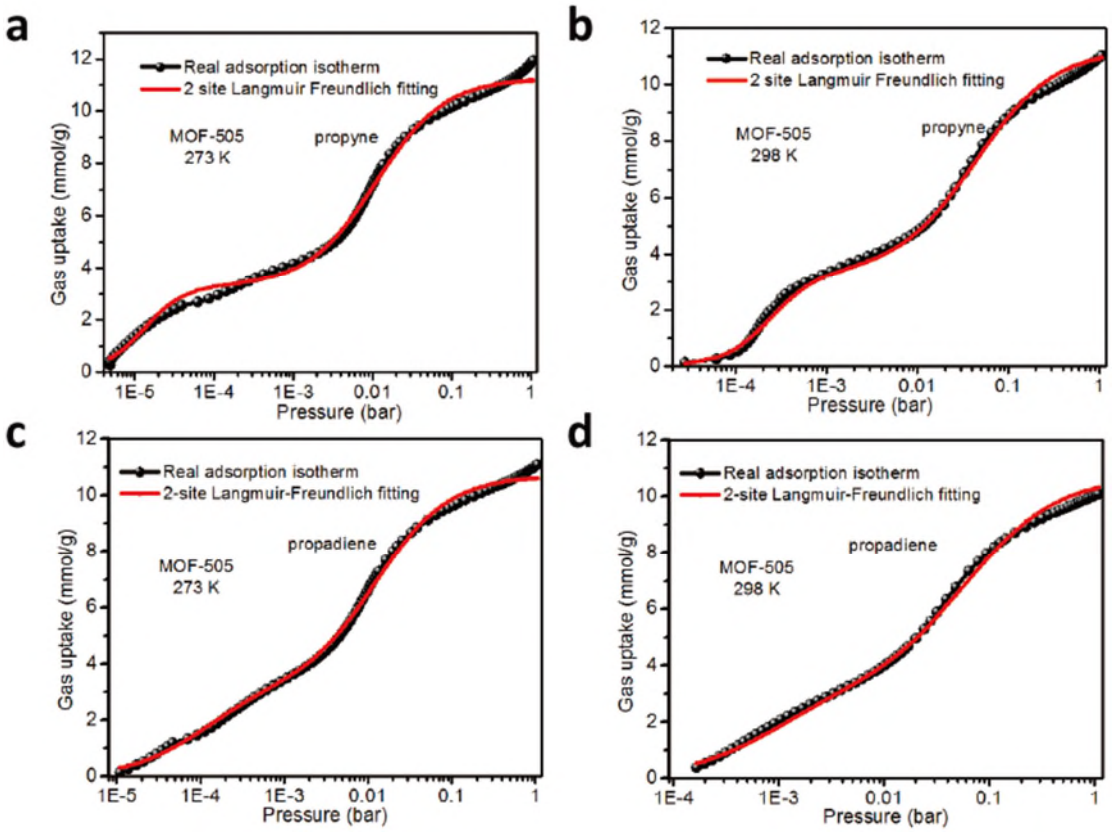

Supplementary Fig. 13 Dual-site Langmuir-Freundlich model fits of propyne and propadiene adsorption isotherms at 273 K and 298 K in MOF-505. **a, b** propyne. **c, d** propadiene.

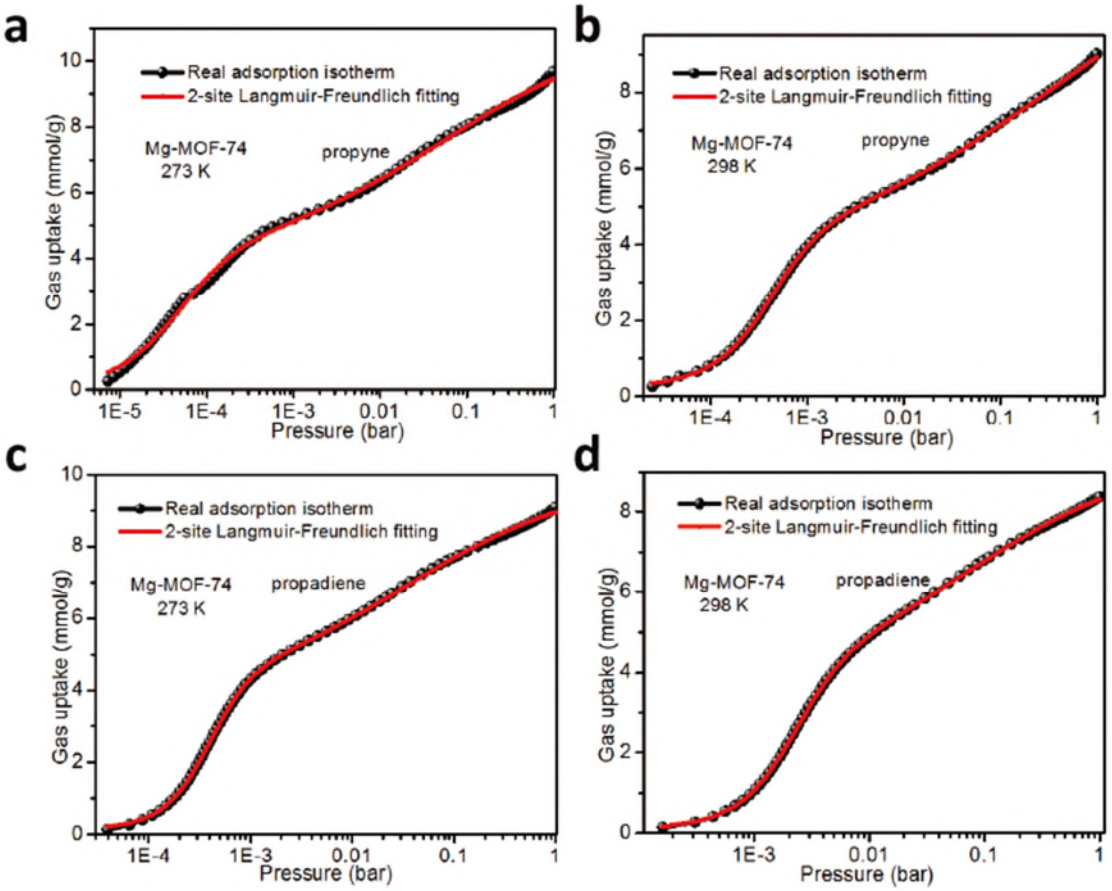

Supplementary Fig. 14 Dual-site Langmuir-Freundlich model fits of propyne and propadiene adsorption isotherms at 273 K and 298 K in Mg-MOF-74. **a, b** propyne. **c, d** propadiene.

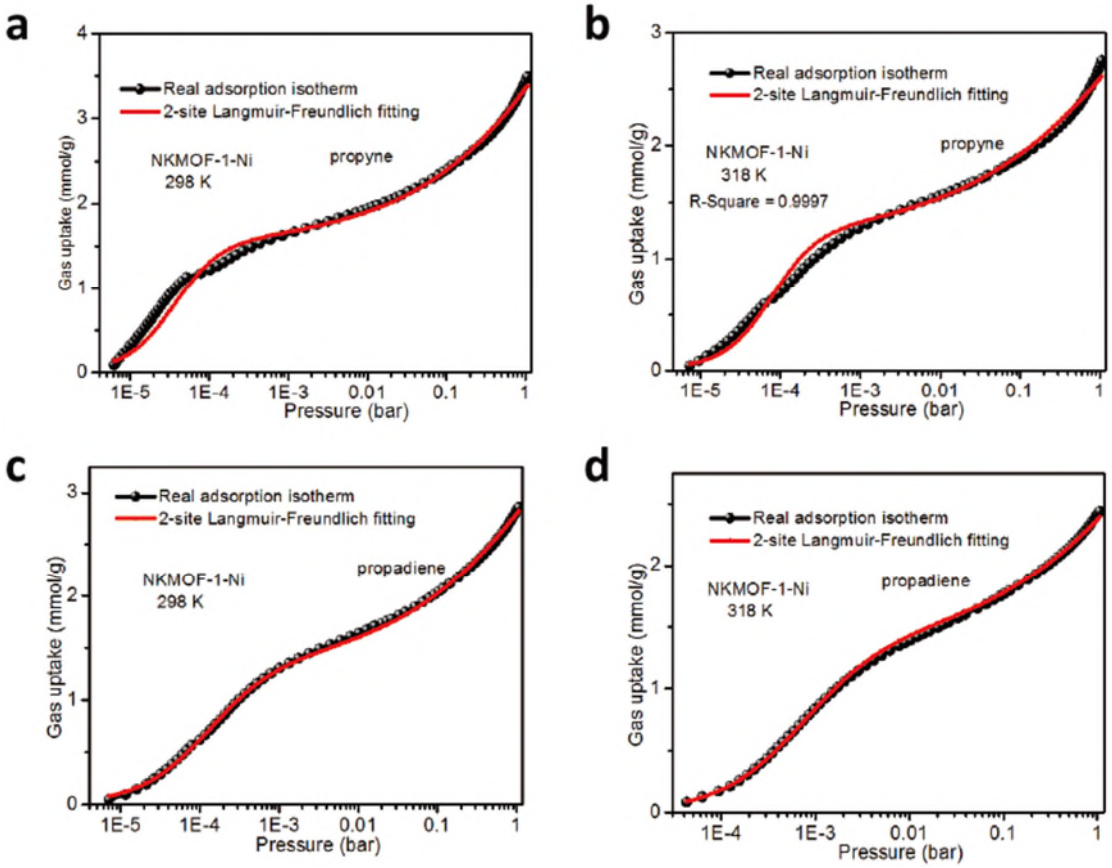

Supplementary Fig. 15 Dual-site Langmuir-Freundlich model fits of propyne and propadiene adsorption isotherms at 273 K and 298 K in NKMOF-1-Ni. **a, b** propyne. **c, d** propadiene.

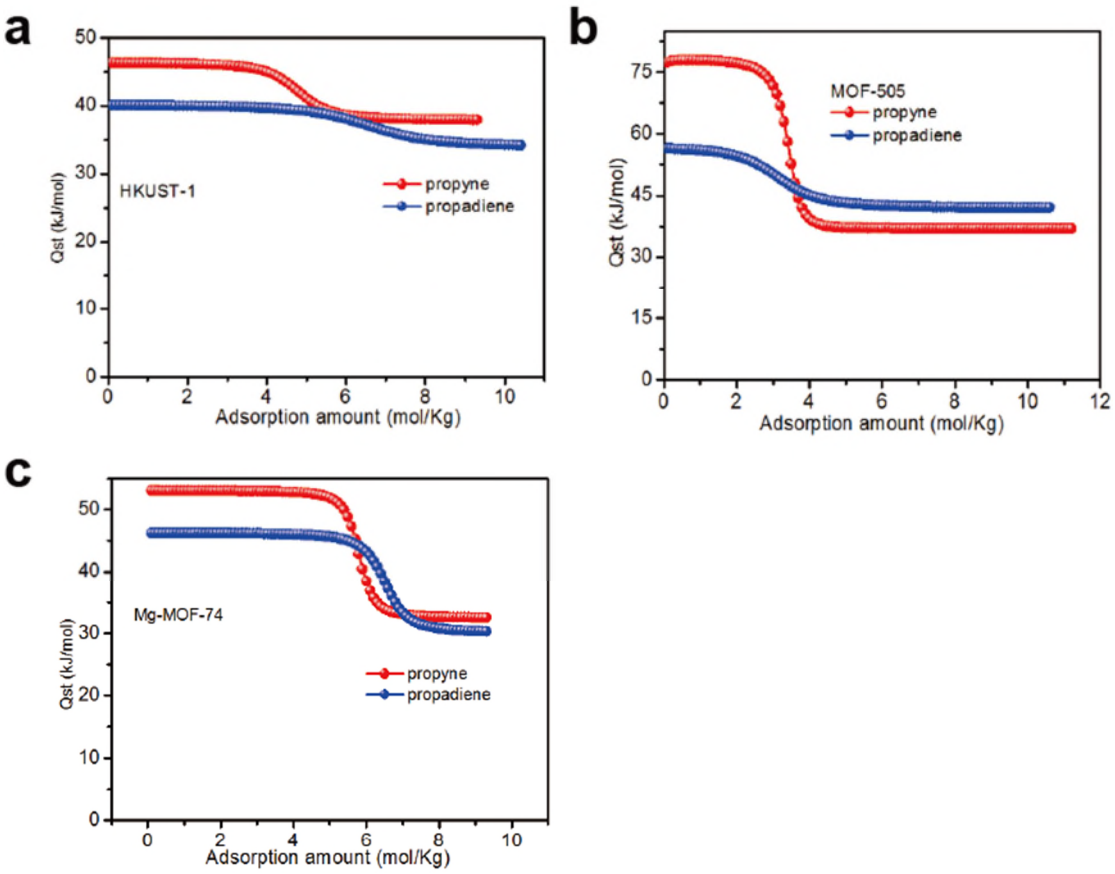

Supplementary Fig. 16 The adsorption isosteric enthalpy (Q_{st}) of propyne and propadiene in (**a**) HKUST-1, (**b**) MOF-505 and (**c**) Mg-MOF-74.

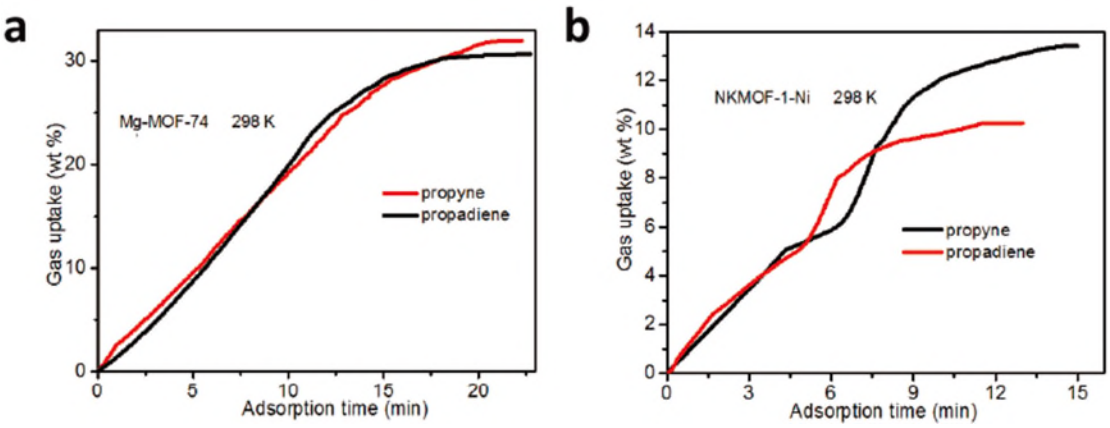

Supplementary Fig. 17 Gravimetric propyne and propadiene sorption kinetics at 298 K. **a** Mg-MOF-74. **b** NKMOF-1-Ni.

Supplementary Table 1. The BET surface, pore size and crystal density of the selected MOFs.

MOF Types	MOFs name	BET surface (m^2/g)	Pore size (Å)	Crystal density (g/cm^3)	Ref
MOFs with open metal sites	HKUST-1	1850	7-10	0.879	(*1*)
	MOF-505	1830	8.3-10.1	0.992	(*2*)
	Mg-MOF-74	1415	11	0.920	(*3*)
	NKMOF-1-Ni	420	5.7	1.12	(*4*)
	MIL-100(Cr)	3100	29	0.784	(*5*)
	MIL-100 (Fe)	2800	32	1.064	(*6*)
	MIL-101(Cr)	4100	29-34	--	(*7*)
MOFs with strong binding sites	SIFSIX-2-Cu-i	735	4.4	1.247	(*8*)
	SIFSIX-3-Ni	250	4.2	1.570	(*9*)
	UTSA-200	612	3.4	1.417	(*10*)
	ZU-62	476	3.2	1.378	(*11*)
MOFs without strong binding sites	UIO-66	1390	6	1.19	(*12*)
	UIO-67	1680	9	1.002	(*12*)
	ZIF-8	1630	3.5	1.067	(*13*)

Supplementary Table 2. Dual-site Langmuir parameter fits for propyne and propadiene in **HKUST-1** at 273 K and 298 K.

Guest	Temperature (K)	Site A		Site B	
		$q_{A,sat}$ (mol Kg^{-1})	B_a (Pa^{-1})	$q_{B,sat}$ (mol Kg^{-1})	b_B (Pa^{-1})
propyne	273	4.8	8.999E-02	6.2	4.727E-04
	298	4.8	1.620E-02	6.2	1.166E-04
propadiene	273	6.5	6.160E-03	4	1.461E-04
	298	6.5	1.394E-03	4	4.165E-05

Supplementary Table 3. Dual-site Langmuir parameter fits for propyne and propadiene in **Mg-MOF-74** at 273 K and 298 K.

Guest	Temperature (K)	Site A		Site B	
		$q_{A,sat}$ (mol Kg^{-1})	b_A (Pa^{-1})	$q_{B,sat}$ (mol Kg^{-1})	b_B (Pa^{-1})
propyne	273	5.8	1.307E-01	3.6	1.865E-04
	298	5.8	1.837E-02	3.6	5.617E-05
propadiene	273	6.5	1.493E-02	2.9	6.081E-05
	298	6.5	2.697E-03	2.9	1.999E-05

Supplementary Table 4. Dual-site Langmuir-Freundlich parameter fits for propyne and propadiene in **MOF-505** at 273 K and 298 K.

Guest	Temperature (K)	Site A			Site B		
		$q_{A,sat}$ (mol Kg^{-1})	b_A (Pa^{-vA})	V_A	$q_{B,sat}$ (mol Kg^{-1})	b_B (Pa^{-vB})	V_B
propyne	273	3.3	6.348E-01	1.7	7.95	9.097E-04	1
	298	3.3	4.484E-03	1.7	7.95	2.317E-04	1
propadiene	273	7.5	7.954E-04	1	3.2	9.413E-02	1
	298	7.5	1.684E-04	1	3.2	1.145E-02	1

Supplementary Table 5. Dual-site Langmuir-Freundlich parameter fits for propyne and propadiene in **NKMOF-1-Ni** at 298 K and 318 K.

Guest	Temperature (K)	Site A			Site B		
		$q_{A,sat}$ (mol Kg^{-1})	b_A (Pa^{-vA})	V_A	$q_{B,sat}$ (mol Kg^{-1})	b_B (Pa^{-vB})	V_B
propyne	298	1.5	1.510E-01	1.48	9	3.651E-03	0.3
	318	1.2	4.788E-02	1.48	4.4	6.526E-03	0.3
propadiene	298	1.35	7.612E-02	1	3.85	3.377E-03	0.4
	318	1.35	1.355E-02	1	3.85	2.032E-03	0.4

Supplementary Table 6: Calculated averaged total potential energies (in kJ mol^{-1}) for a single propyne and propadiene molecule, individually, positioned about the open-metal sites in **HKUST-1**, **MOF-505**, and **Mg-MOF-74** and within the tetrahedral cage in **HKUST-1** as determined from CMC simulations at 298 K/0.10 atm.

MOF	Adsorbate	MOF-Adsorbate Energy (kJ mol^{-1})
HKUST-1	Propyne (Open-Metal Site)	– 54.15
	Propadiene (Open-Metal Site)	– 50.74
	Propyne (Tetrahedral Cage)	– 47.37
	Propadiene (Tetrahedral Cage)	– 48.85
MOF-505	Propyne	– 89.17
	Propadiene	– 43.19
Mg-MOF-74	Propyne	– 78.46
	Propadiene	– 60.62

Supplementary References

1. Lin, Kuen-Song, *et al*. Synthesis and characterization of porous HKUST-1 metal organic frameworks for hydrogen storage. *Int. J. Hydrogen. Energy.* **37,** 13865-13871 (2012).

2. Chen, B. *et al.* High H_2 adsorption in a microporous metal-organic framework with open metal sites. *Angew. Chem., Int. Ed.* **44**, 4745-4749 (2005).

3. Caskey, S. R., Wong-Foy, A. G. & Matzger, A. J. Dramatic tuning of carbon dioxide uptake via metal substitution in a coordination polymer with cylindrical pores. *J. Am. Chem. Soc*. **130**, 10870-10871 (2008).

4. Peng, Y. L. *et al*. A robust heterometallic ultramicroporous MOF with ultrahigh selectivity for propyne/propylene separation. *J. Mater. Chem. A,* **9**, 2850-2856 (2021).

5. Férey, G. *et al.* A hybrid solid with giant pores prepared by a combination of targeted chemistry, simulation, and powder diffraction. *Angew. Chem., Int. Ed.* **116**, 6456-6461(2004).

6. Horcajada, P. *et al.* Synthesis and catalytic properties of MIL-100 (Fe), an iron (III) carboxylate with large pores. *Chem. Commun.* **27**, 2820-2822 (2007).

7. Férey, G. *et al.* A chromium terephthalate-based solid with unusually large pore volumes and surface area. *Science* **309**, 2040-2042 (2005).

8. Nugent, P. *et al.* Porous materials with optimal adsorption thermodynamics and kinetics for CO_2 separation. *Nature* **495**, 80-84 (2013).

9. Kumar, A. *et al.* Direct air capture of CO_2 by physisorbent materials. *Angew. Chem.,*

Int. Ed. **54**, 14372-14377 (2015).

10. Li, B. *et al.* An ideal molecular sieve for acetylene removal from ethylene with record selectivity and productivity. *Adv. Mater.* **29**, 1704210 (2017).
11. Yang, L. *et al.* An asymmetric anion-pillared Metal-organic framework as a multisite adsorbent enables simultaneous removal of propyne and propadiene from propylene. *Angew. Chem., Int. Ed.* **130**, 13329-13333 (2018).
12. Cavka, J. H. *et al.* A new zirconium inorganic building brick forming metal organic frameworks with exceptional stability. *J. Am. Chem. Soc*. **130**, 13850-13851 (2008).
13. Park, K. S. *et al.* Exceptional chemical and thermal stability of zeolitic imidazolate frameworks. *Proc. Natl. Acad. Sci.* **103**, 10186-10191 (2006).
14. Krishna, R. The maxwell-stefan description of mixture diffusion in nanoporous crystalline materials. *Micropor. mesopo. mat.* **185**, 30-50 (2014).
15. Krishna, R. Methodologies for evaluation of Metal‐organic frameworks in separation applications. *RSC Adv.* **5**, 52269-52295 (2015).

15. Krishna, R. Screening metal-organic frameworks for mixture separations in fixed-bed adsorbers using a combined selectivity/capacity metric. *RSC Adv.* **7**, 35724-35737 (2017).

16. Krishna, R. Methodologies for screening and selection of crystalline microporous materials in mixture separations. *Sep. Purif. Technol.* **194**, 281-300 (2018).

17. Krishna, R. Metrics for evaluation and screening of metal-organic frameworks for applications in mixture separations. ACS Omega 5, 16987-17004 (2020).

18. Chui, S. S. Y., Lo, S. M. F., Charmant, J. P., Orpen, A. G. & Williams, I. D. A chemically functionalizable nanoporous material $[Cu_3(TMA)_2(H_2O)_3]$ n. *Science* **283**, 1148-1150 (1999).

19. Chen, B. *et al.* High H_2 adsorption in a microporous metal-organic framework with open metal sites. *Angew. Chem. Int. Ed.* **44**, 4745-4749 (2005).

20. Pham, T. *et al.* Understanding the H_2 sorption trends in the M-MOF-74 series (M= Mg, Ni, Co, Zn). *J. Phys. Chem. C* **119**, 1078-1090 (2015).

21. Lennard-Jones, J. E. On the determination of molecular fields. II. From the equation of state of gas. *Proc. Roy. Soc. A* **106**, 463-477 (1924).

22. Rappé, A. K. *et al.* UFF, a full periodic table force field for molecular mechanics and molecular dynamics simulations. *J. Am. Chem. Soc*. **114**, 10024-10035 (1992).

23. Valiev, M. *et al.* NWChem: A comprehensive and scalable open-source solution for large scale molecular simulations. *Comput. Phys. Commun.* **181**, 1477-1489 (2010).

24. Cornell, W. D. *et al.* A second generation force field for the simulation of proteins, nucleic acids, and organic molecules *J. Am. Chem. Soc.* **117**, 5179-5197 (1995).

25. Stevens,W. J., Basch, H. & Krauss, M. Compact effective potentials and efficient shared-exponent basis sets for the first-and second-row atoms. *J. Chem. Phys.* **81**, 6026-6033 (1984).

26. Hay, P. J., Wadt, W. R. Ab initio effective core potentials for molecular calculations. Potentials for the transition metal atoms Sc to Hg. *J. Chem. Phys.* **82**, 270-283 (1985).

27. LaJohn, L. A., Christiansen, P. A., Ross, R. B., Atashroo, T. & Ermler, W. C. A binitio relativistic effective potentials with spin-orbit operators. III. Rb through Xe. *J. Chem. Phys.* **87**, 2812-2824 (1987).

28. Duijnen, P. T. V. & Swart, M. Molecular and atomic polarizabilities: Thole's model revisited. *J. Phys. Chem. A* **102**, 2399-2407 (1998).

29. Forrest, K. A. *et al.* Simulation of the mechanism of gas sorption in a Metal‐organic framework with open metal sites: Molecular hydrogen in PCN-61. *J. Phys. Chem. C* **116**, 15538-15549 (2012).

30. Peng,Y.-L. *et al.* Robust microporous metal-organic frameworks for highly efficient and simultaneous removal of propyne and propadiene from propylene *Angew. Chem. Int. Ed.* **58**, 10209-10214 (2019).

31. Ewald, P. P. Die Berechnung optischer und elektrostatischer Gitterpotentiale. *Ann. Phys.* **369**, 253-287(1921).

32. Wells, B. A. & Chaffee, A. L. Ewald summation for molecular simulations. *J. Chem. Theory Comput.* **11**, 3684-3695 (2015).

33. Applequist, J., CarlK. J. R. & Fung, K. Atom dipole interaction model for molecular polarizability. Application to polyatomic molecules and determination of atom polarizabilities. *J. Am. Chem. Soc.* **94**, 2952-2960 (1972).

34. Thole, B. T. Molecular polarizabilities calculated with a modified dipole interaction. *Chem. Phys.* 59, 341-350 (1981).

35. Bode,K. A. & Applequist, J. A new optimization of atom polarizabilities in halomethanes, aldehydes, ketones, and amides by way of the atom dipole

interaction model. *J. Phys. Chem.* **100**, 17820-17824 (1996).

36. McLaughlin, K., Cioce, C. R., Pham, T., Belof, J. L. & Space, B. Efficient calculation of many-body induced electrostatics in molecular systems. *J Chem Phys* 139, 184112 (2013).

37. Belof, J. L. & Space, B. Massively Parallel Monte Carlo (MPMC). Available on GitHub. https://github.com/mpmccode/mpmc (2012).

38. Franz, D. M. *et al.* MPMC and MCMD: Free High-Performance Simulation Software for Atomistic Systems. *Adv. Theory Simul.* **2**, 1900113 (2019).

39. Kirkpatrick, S., Gelatt, C. D., Vecchi, M. P. Optimization by simulated annealing. *Science* **220**, 671-680 (1983).

40. Frenkel, D., Smit, B. (2002). *Understanding Molecular Simulation: From Algorithms to Applications. Chapter 5* (New York, p112 – p114, 2002)